

The Impact of Cold-Air Outbreaks and Oceanic Lateral Fluxes on Dense-Water Formation in the Greenland Sea from a 10-Year Moored Record (1999–2009)

KRISTIN SVINGEN,^{a,b} AILIN BRAKSTAD,^{a,b} KJETIL VÅGE,^{a,b} WILKEN-JON VON APPEN,^c AND LUKAS PAPRITZ^d

^a *Geophysical Institute, University of Bergen, Bergen, Norway*

^b *Bjerknes Centre for Climate Research, Bergen, Norway*

^c *Alfred Wegener Institute, Helmholtz Centre for Polar and Marine Research, Bremerhaven, Germany*

^d *Institute of Atmospheric and Climate Science, Department of Environmental System Science, ETH Zurich, Zurich, Switzerland*

(Manuscript received 29 July 2022, in final form 1 March 2023, accepted 5 March 2023)

ABSTRACT: The Greenland Sea produces a significant portion of the dense water from the Nordic seas that supplies the lower limb of the Atlantic meridional overturning circulation. Here, we use a continuous 10-yr hydrographic record from moored profilers to examine dense-water formation in the central Greenland Sea between 1999 and 2009. Of primary importance for dense-water formation is air–sea heat exchange, and 60%–80% of the heat lost to the atmosphere during winter occurs during intense, short-lived events called cold-air outbreaks (CAOs). The long duration and high temporal resolution of the moored record has for the first time facilitated a statistical quantification of the direct impact of CAOs on the wintertime mixed layer in the Greenland Sea. The mixed layer development can be divided into two phases: a cooling phase and a deepening phase. During the cooling phase (typically between November and January), CAOs cooled the mixed layer by up to 0.08 K day^{-1} , depending on the intensity of the events, while the mixed layer depth remained nearly constant. Later in winter (February–April), heat fluxes during CAOs primarily led to mixed layer deepening of up to 38 m day^{-1} . Considerable variability was observed in the mixed layer response, indicating that lateral fluxes of heat and salt were also important. The magnitude and vertical distributions of these fluxes were quantified, and idealized mixed layer simulations suggest that their combined effect is a reduction in the mixed layer depth at the end of winter of up to several hundred meters.

KEYWORDS: Arctic; In situ oceanic observations; Deep convection; Oceanic mixed layer; Air–sea interaction; Cold air surges


1. Introduction

The Atlantic meridional overturning circulation plays a crucial role in global climate. Warm and saline Atlantic Water (AW) is transported from the equator toward higher latitudes by the upper branch of the circulation. On its way poleward, heat is lost to the atmosphere. This transforms the water into colder and denser water masses that return equatorward at depth. The majority of the overturning takes place east of Greenland (Lozier et al. 2019; Petit et al. 2020). The densest component is formed in the Nordic seas (comprising the Greenland, Iceland, and Norwegian Seas, Fig. 1) and spills across the Greenland–Scotland Ridge into the deep North Atlantic. While descending, the overflow plumes entrain surrounding water masses, which together supply the lower branch of the overturning circulation (Chafik and Rossby 2019).

One important mechanism of dense-water formation in the Nordic seas is open-ocean convection. This takes place within the cyclonic Greenland Sea Gyre, where doming of dense isopycnals reduces stratification and preconditions the water

column for wintertime convection (e.g., Marshall and Schott 1999). The Greenland Sea Gyre also experiences severe heat loss to the atmosphere during winter (Moore et al. 2015). The cooling and densification of the surface layer initiates convective overturning and the production of dense water. Approximately 60%–80% of the total heat lost to the atmosphere in this region during winter occurs during intense, short-lived cold-air outbreaks (CAOs; Papritz and Spengler 2017). Marine CAOs occur when cold polar air masses over land and ice are advected over relatively warm water, leading to large ocean to atmosphere heat fluxes near the sea-ice edge. Over the past 50 years the sea-ice edge has retreated toward Greenland, which has led to a reduced intensity of CAOs and an overall decline in winter heat loss over the gyre (Moore et al. 2015; Somavilla 2019; Dahlke et al. 2022; Moore et al. 2022). This has, and is projected to continue having, substantial ramifications for water-mass transformation in the central Greenland Sea.

Prior to 1980, deep-reaching convection in the central Greenland Sea produced cold and dense Greenland Sea Deep Water (GSDW), which was considered the main source of deep water in the Nordic seas (Helland-Hansen and Nansen 1909; Malmberg 1983; Aagaard et al. 1985). There is no evidence of significant renewal of GSDW after the early 1980s, and the main product of convection since then has been the warmer, saltier, and less dense Greenland Sea Arctic Intermediate Water (GSAIW; Meincke et al. 1990, 1997; Karstensen et al. 2005; Ronski and Budéus 2005; Latarius and Quadfasel 2010; Brakstad et al. 2019). Convection has been limited to

 Denotes content that is immediately available upon publication as open access.

Kristin Svingen and Ailin Brakstad contributed equally to this paper and should be considered co-first authors.

Corresponding author: Ailin Brakstad, ailin.brakstad@uib.no

DOI: 10.1175/JPO-D-22-0160.1

© 2023 American Meteorological Society. For information regarding reuse of this content and general copyright information, consult the [AMS Copyright Policy \(www.ametsoc.org/PUBSReuseLicenses\)](https://www.ametsoc.org/PUBSReuseLicenses).

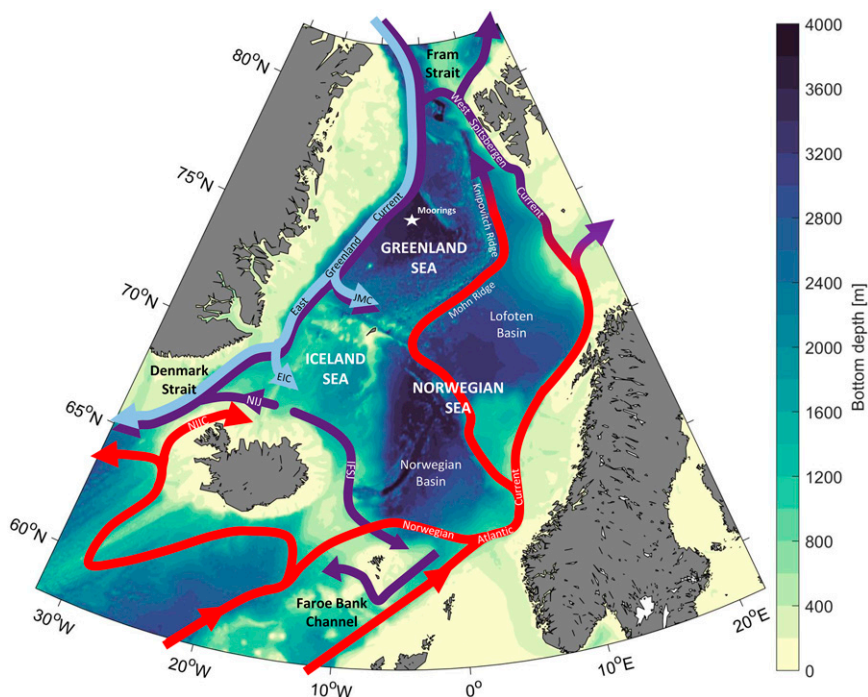


FIG. 1. Schematic circulation in the Nordic seas. The red arrows indicate inflow of warm Atlantic Water, the dark purple arrows mark the flow of dense water, and the light blue arrows show the flow of Polar Surface Water. The location of the moorings is indicated by the white star. The acronyms are the North Icelandic Irminger Current (NIIC), the North Icelandic Jet (NIJ), the Iceland–Faroe Slope Jet (IFSJ), the East Icelandic Current (EIC), and the Jan Mayen Current (JMC).

less than 2000-m depth, and an intermediate stratification maximum (that has further isolated the GSDW from the surface) has developed. The formation of GSDW ceased as a result of reduced atmospheric forcing, combined with temporary freshening that enhanced the stability of the gyre and less local sea-ice formation (Meincke et al. 1992; Visbeck et al. 1995; Somavilla 2019). According to Moore et al. (2015, 2022), the trend toward weaker atmospheric heat fluxes over the Greenland Sea is expected to continue in a warming climate with continued sea-ice retreat. This has not yet limited GSAIW formation, primarily due to increased salt advection into the Greenland Sea since the mid-1990s, resulting in higher densities and a tendency for deeper convection (Lauvset et al. 2018; Brakstad et al. 2019). The overall magnitudes of heat (57 W m^{-2}) and freshwater ($-21 \text{ mm month}^{-1}$) fluxes into the central Greenland Sea were estimated by Latarius and Quadfasel (2016) based on budget calculations. However, uncertainties remain regarding their vertical distributions and where the heat and salt enter the gyre.

While wintertime convection in the Greenland Sea presently produces only intermediate water, this water mass can more directly contribute to the dense overflow waters spilling across the Greenland–Scotland Ridge from the Nordic seas into the deep North Atlantic. Roughly 90% of the dense water emanating from the Nordic seas passes the ridge through either Denmark Strait or the Faroe Bank Channel (FBC; Østerhus et al. 2019). Two main currents supply the Denmark

Strait overflow: the East Greenland Current (EGC) and the North Icelandic Jet (NIJ; Harden et al. 2016; Våge et al. 2011). The overflow water transported with the EGC is mainly Atlantic-origin water that has been gradually cooled and densified along its path around the rim of the Nordic seas and Arctic Ocean (Mauritzen 1996; Eldevik et al. 2009; Våge et al. 2018; Håvik et al. 2019), but also a nonnegligible portion of water formed in the Greenland Sea (Strass et al. 1993; Jeansson et al. 2008). The NIJ, on the other hand, transports water formed primarily in the Greenland Sea (Semper et al. 2019; Huang et al. 2020; Våge et al. 2022; Brakstad et al. 2023). The total contribution from the Greenland Sea to the Denmark Strait overflow is $39\% \pm 2\%$ (Brakstad et al. 2023). The Greenland Sea is also an important source of the Iceland–Faroe Slope Jet that, together with dense water flowing southward along the Jan Mayen Ridge, supply overflow water to the FBC (Semper et al. 2020; Huang et al. 2020; Chafik et al. 2020; Brakstad et al. 2023). In total, $46\% \pm 8\%$ of the FBC overflow originates in the Greenland Sea, while the other main source is the Arctic Ocean (Brakstad et al. 2023). This is in line with Jeansson et al. (2017), who focused on the origin of the intermediate water in the Norwegian Sea upstream of the FBC. The Greenland Sea is thus an important source of overflow water both east and west of Iceland.

Even though water-mass transformation in the Greenland Sea has been an active topic of investigation for several decades (e.g., Meincke et al. 1990, 1992; Ronski and Budéus 2005;

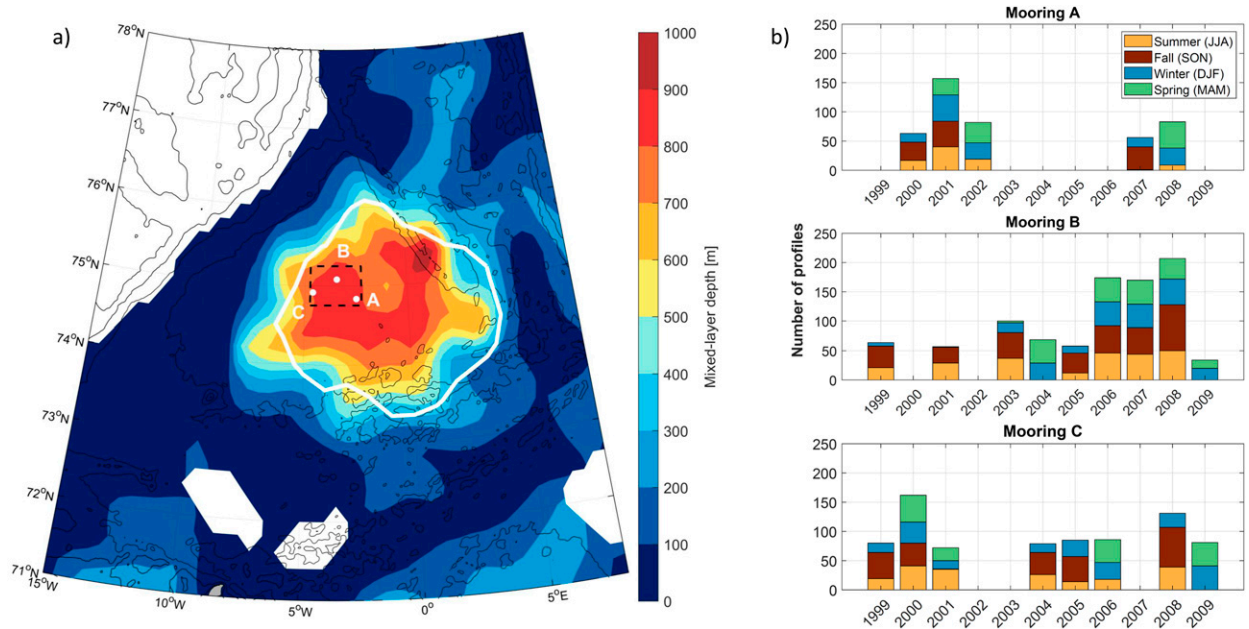


FIG. 2. (a) The locations of moorings A, B, and C. The colors show mean late-winter (February–April) mixed layer depth from the winters with the 30% deepest convection depths between 1986 and 2016 (based on Fig. 3c in Brakstad et al. 2019). The black contours show the 250-, 500-, 1000-, 2000-, and 3000-m isobaths. The outline of the Greenland Sea Gyre as defined by Moore et al. (2015) using dynamic topography of the sea surface relative to 500-m depth is indicated by the white contour. The black dashed line outlines the area over which ERA5 data were averaged. (b) The number of hydrographic profiles each year sorted by mooring and season.

Latarius and Quadfasel 2010; Brakstad et al. 2019; Somavilla 2019), most studies have focused on interannual and long-term variability. Here we use a set of three profiling moorings that were deployed within the Greenland Sea Gyre from 1999 to 2009 to investigate the wintertime evolution of the mixed layer. The profilers measured temperature, salinity, and pressure nearly from the surface to the bottom on average every second day (daily between 2008 and 2009). Due to the long duration and high temporal resolution of the data, we could quantify the direct impact of CAOs on the wintertime mixed layer using a statistical approach, and, in particular, how the response depended on the timing and intensity of the events. This has not previously been possible due to sparse data coverage and the short duration of CAOs (Terpstra et al. 2021). In addition to the impact of atmospheric forcing, previous studies have highlighted the importance of lateral heat and salt fluxes (e.g., Latarius and Quadfasel 2016; Lauvset et al. 2018; Brakstad et al. 2019). We determined the vertical distribution of the lateral heat and salt fluxes into the central Greenland Sea, and used that information in idealized numerical simulations to investigate their impact on the wintertime development of the mixed layer.

2. Data and methods

a. Hydrographic data

Our analysis is primarily based on 10 years (1999–2009) of hydrographic measurements from three moored profilers in the central Greenland Sea. The moorings, hereafter referred to as moorings A (74°50'N, 2°30'W), B (75°05'N, 3°27'W),

and C (74°55'N, 4°37'W), were all located within the cyclonic Greenland Sea Gyre (Fig. 2a), where Brakstad et al. (2019) found the deepest and densest wintertime mixed layers.

Each moored profiler was recovered and redeployed every summer. They were equipped with Sea-Bird Electronics SBE19 Seacats that measured conductivity, temperature, and pressure from approximately 100 m below the sea surface to a few meters above the sea floor at ~3700 m every second day. It requires a large amount of power to operate a profiling vehicle over a year. To overcome challenges related to energy consumption, the vertical motion of the profiler was driven by changes in buoyancy by adding and removing lead weights from the vehicle. The lead weights were kept in a basket mounted at the top of the mooring. The profiler itself was buoyant, and for each cycle the profiler was ballasted by a lead weight from the basket. The additional weight decreased the buoyancy of the vehicle and caused it to sink to the sea floor. At the bottom of the mooring, the lead weight was unloaded and the vehicle returned to the surface driven by its own positive buoyancy. Measurements were only taken during the dive, when the profiler reached a downward velocity of 0.8–1.0 m s⁻¹ (Budéus et al. 2005). Temperature and conductivity were measured at a frequency of 1 Hz, which corresponds to a vertical resolution of approximately 1 m, while pressure was recorded every 120 s. The initial accuracy of the instrument was 0.005°C for temperature and 0.0005 S m⁻¹ for conductivity. For the temperatures in the Greenland Sea, this corresponds to a salinity accuracy better than 0.01 g kg⁻¹. Additional technical details regarding the mooring configuration and performance can be found in Budéus et al. (2005).

The postprocessing included calibration of the mooring data against shipboard CTD measurements collected from the annual mooring turnaround cruises, smoothing of the profiles with a 10-m median filter, and interpolation of the data to integer pressure values. Values outside the expected range of temperature and salinity in the Nordic seas of $[-2, 20]^{\circ}\text{C}$ and $[20, 36] \text{ g kg}^{-1}$, respectively (e.g., Våge et al. 2013) were excluded. The total coverage of quality-controlled data from each mooring is shown in Fig. 2b. Vertical profiles were generally obtained every second day, except during 2008–09 when daily profiles were collected. However, due to technical issues the profilers were at times parked at a constant depth. This was caused either by problems with the loading/unloading of the lead weights that on 11 occasions lasted for the entire deployment, or shorter periods when profiling was prevented by strong currents (Budéus et al. 2005; Budéus 2009). Measurements taken during these periods were not considered.

Data from all three moorings were combined in order to obtain one complete time series from 1999 to 2009 with the minimal number of gaps due to missing data. Before combining the data, mixed layer depths and hydrographic properties, as well as hydrographic properties at depth (2000 m), were compared between moorings that had collected data simultaneously (not shown). Both the end-of-winter mixed layer depths and the monthly mean mixed layer properties agreed well between the different mooring locations. The largest differences in monthly mean mixed layer depth occurred in late winter (March and April), mainly caused by variations in the onset of restratification at the different mooring locations. The differences between monthly mean hydrographic properties at 2000-m depth were negligible. The mooring locations are hereafter used interchangeably to represent the general conditions within the Greenland Sea Gyre. Data from mooring B were used as the basis for the combined time series. Data gaps were filled using data from the other two moorings.

The delicate construction of the buoyant profiler inhibited measurements close to the surface (Budéus et al. 2005; Budéus 2009). The shallowest depths of the profiles varied between deployments, from 95 to 185 m. In the final year of the deployment period (2008–09) a supplementary mooring was deployed to cover the upper part of the water column, from the surface to 130 m. This mooring was located 1.8 km away from mooring C. To overcome the influence of surface waves, this profiler had much greater positive buoyancy than the deep profilers. The surface profiler was equipped with a Sea-Bird Electronics SBE41, which has an initial accuracy of 0.002°C and 0.002 g kg^{-1} for temperature and salinity, respectively. Measurements from moorings B and C were combined with surface measurements from the supplementary mooring to form surface to bottom profiles. The transition between the upper and lower datasets was not smoothed and the profiles from 2008 to 2009 have a distinct joint at 130 m. Further details about the 2008–09 deployment can be found in a technical report (Budéus 2009).

In addition to the mooring data, we used hydrographic profiles from 1999 to 2012 from a database collected by Brakstad et al. (2023). This database consists of profiles from various archives over the period 1950–2019 covering the domain 50° – 90°N and 45°W – 65°E . The majority of the data collected

in the Greenland Sea during this period was obtained from the Unified Database for Arctic and Subarctic Hydrography (UDASH; Behrendt et al. 2018) and consists of shipboard hydrographic measurements and Argo float profiles.

Following the new standard of the International Thermodynamic Equation Of Seawater-2010 (TEOS-10; IOC et al. 2010) Conservative Temperature and Absolute Salinity (hereafter referred to as temperature and salinity, respectively) were calculated from all hydrographic data and used throughout the analysis.

b. Mixed layer depths

Apart from the 2008–09 deployment, the moored profilers did not measure the upper 100 m of the water column. Hence, only mixed layers extending well below this depth could be identified. In total, mixed layers were identified in 49% of the profiles. The remaining profiles were mainly from summer when the mixed layer was too shallow to be detected.

Depth and properties of the mixed layer were determined using a robust procedure previously applied by Våge et al. (2015) and Brakstad et al. (2019). The mixed layer depth was first estimated by two automated routines, one based on the curvature of the temperature profile (Lorbacher et al. 2006) and the other based on a density difference criterion (Nilsen and Falck 2006). Each profile and the corresponding mixed layer depth estimates were then visually inspected. One or both of the automated routines accurately determined the mixed layer depth for approximately half of the profiles where the mixed layer was sufficiently deep to reach the moorings. For the remaining profiles, a manual procedure developed by Pickart et al. (2002) was applied. The extent of the mixed layer was first estimated visually, and the means and standard deviations of the mixed layer temperature, salinity, and density were calculated over this depth range. Finally, the top and bottom of the mixed layer were determined as the depths where either the temperature, salinity, or density profile permanently exceeded two standard deviations from the mean.

The manual procedure was also used for the majority of the combined profiles from 2008 to 2009 because of the distinct joint at 130 m. The small shift in hydrographic properties between the deep and the shallow profilers was due to their lateral displacement. When the mixed layer extended beneath the shallow moored profiler, the manual procedure was used to set the upper limit of the mixed layer below the joint, even though the mixed layer extended to the surface. This ensured that mixed layer properties were estimated based on data only from the deep profiler. When the mixed layer was shallower than 130 m and fully in the range of the shallow profiler, the automated routines generally performed well.

c. Atmospheric data

Hourly atmospheric fields were obtained from the ERA5 reanalysis, which is the fifth-generation reanalysis produced by the European Centre for Medium-Range Weather Forecasts (Hersbach et al. 2020). The reanalysis data have first been interpolated to a 0.25° latitude–longitude grid and then averaged over a box enclosing all three moorings (74.75° – 75.25°N and 2.25° – 4.75°W ; Fig. 2a). We used analyzed fields

of potential temperature at 900 hPa, surface skin temperature, surface pressure, and sea-ice concentration, as well as short-range forecasts of wind stress, surface sensible and latent turbulent heat fluxes, evaporation, precipitation, and long- and shortwave radiation.

d. Cold-air outbreaks

To identify CAO events, we followed previous works (e.g., Bracegirdle and Gray 2008; Kolstad 2011; Papritz et al. 2015; Fletcher et al. 2016; Papritz and Spengler 2017; Terpstra et al. 2021) by using a CAO index defined as the difference between potential skin water temperature (θ_{SKT}) and potential air temperature at 900 hPa ($\theta_{900\text{hPa}}$), i.e., $\theta_{\text{SKT}} - \theta_{900\text{hPa}}$. Papritz and Spengler (2017) found that CAOs with a CAO index in excess of 4 K are closely associated with enhanced upward turbulent heat fluxes and are, therefore, most relevant for dense-water formation in the western Nordic seas. Consequently, time steps with a CAO index below 4 K were not considered. From the CAO index time series, the cold-air outbreaks each winter were identified on an event by event basis as follows: The peak of the first event was defined as the maximum CAO index. Every neighboring data point with a CAO index higher than 4 K was then assigned to that event. The start and end of the event were set to the first and last data points where the CAO index was higher than 4 K. Further events were then identified iteratively following the same procedure by considering only data points that were not yet attributed to another event. In the end all events with peak values exceeding 4 K were identified, and all data points with a CAO index higher than 4 K were assigned to a particular event. Following Papritz and Spengler (2017), each event was classified as either moderate ($4 \text{ K} < \theta_{\text{SKT}} - \theta_{900\text{hPa}} \leq 8 \text{ K}$), strong ($8 \text{ K} < \theta_{\text{SKT}} - \theta_{900\text{hPa}} \leq 12 \text{ K}$), or very strong ($12 \text{ K} < \theta_{\text{SKT}} - \theta_{900\text{hPa}}$) according to the peak value of the CAO index. The temporal distribution of turbulent heat fluxes during the events (centered at the peak CAO index) is shown in Fig. 3 for each intensity class. Both the length of the event and the peak turbulent heat flux increase with CAO intensity.

Terpstra et al. (2021) found that the median duration of a CAO in this region is 2.5 days, with lower and upper quartiles of 1.8 and 4.1 days. To quantify the direct impact of CAOs on the wintertime mixed layer we therefore investigated profile-to-profile changes in mixed layer depth and temperature between all profiles obtained 4 days or less apart. Profiles where the mixed layer was not detected by the moorings were excluded from the analysis. The changes were calculated separately at each of the three mooring locations and divided by the time span between the profiles to estimate a daily rate of change. Each of these differences in mixed layer properties were grouped according to the CAO intensity classification above by the median value of the CAO index between the profiles.

e. Idealized mixed layer model

To investigate how the timing of CAOs and oceanic lateral advection impact the mixed layer development, we employed a one-dimensional mixed layer model known as the Price–Weller–

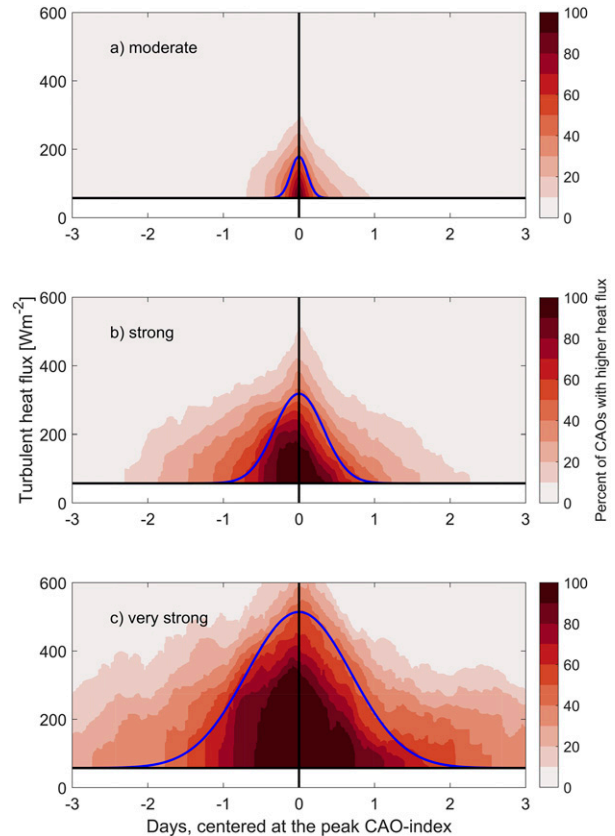


FIG. 3. Temporal distribution of turbulent heat fluxes during (a) moderate, (b) strong, and (c) very strong CAOs. All CAOs were centered at the peak CAO index. The color indicates the percentage of CAO events exceeding the turbulent heat flux value on the y axis. The black horizontal lines mark the winter mean background turbulent heat flux when no CAO was present (57 W m^{-2}). The blue curves are idealized CAOs with a Gaussian distribution (section 2e).

Pinkel (PWP) model after Price et al. (1986). A modified version of this model, including lateral fluxes of heat and salt, was developed by Moore et al. (2015) and Brakstad et al. (2019) to better represent the conditions in the central Greenland Sea. Lateral advection of heat was parameterized by Moore et al. (2015) based on the annual-mean heat budget for the Greenland Sea Gyre and reflects the vertical profile of the temperature difference across the gyre boundary. The same principle was used to parameterize lateral advection of salt by Brakstad et al. (2019), who also included salt fluxes from formation of sea ice. In this study, we updated the PWP model setup for the Greenland Sea with our improved estimates of lateral heat and salt fluxes (section 6). The importance of lateral advection was examined by comparing two sets of PWP runs for each winter (one with and one without lateral advection) to the observed mixed layer evolution. The initial hydrographic conditions were based on the first November profile where the mixed layer was detected by the moorings. The model was then integrated to the end of April with realistic atmospheric forcing based on hourly heat,

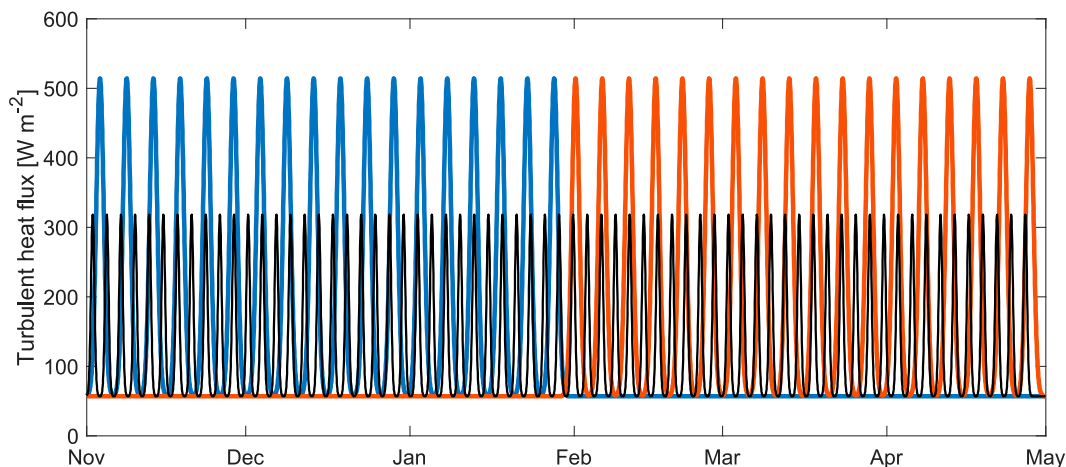


FIG. 4. Time series of turbulent heat fluxes for idealized CAOs concentrated early in winter (blue), late in winter (orange), and evenly distributed throughout winter (black). These were constructed based on the idealized heat-flux distributions for single CAOs (blue curves, Fig. 3) as described in the text. The integrated November–April heat loss equals the 1999–2009 mean for all three time series, while the background heat flux without CAOs is 57 W m^{-2} .

freshwater, and momentum fluxes from ERA5 (section 2c). We note that sea surface temperatures below the freezing point were nearly absent during the time period considered here. Hence, the effect of salt fluxes from sea-ice formation was negligible. The model has a vertical resolution of 2 m and a time step of 1 h.

The same setup, but with idealized atmospheric forcing, was used to examine how the timing of CAOs impacts the mixed layer development. To isolate the effect of the temporal CAO distribution, we required that the integrated turbulent heat loss from November to April was equal to the 1999–2009 mean in all simulations. Three different cases were then considered: one with all CAOs concentrated early in winter, one with all CAOs concentrated late in winter, and one with CAOs evenly distributed throughout the winter. The corresponding time series of turbulent heat fluxes (Fig. 4) were constructed based on idealized heat-flux distributions of single CAOs (blue curves in Fig. 3). The idealized CAOs have Gaussian distributions with peak turbulent heat fluxes (181, 318, and 515 W m^{-2}) and durations (0.7, 2.7, and 5.0 days) equal to the means of the moderate, strong, and very strong events, respectively (section 2d). The background turbulent heat flux when the CAO index was below 4 K was 57 W m^{-2} on average (black horizontal lines in Fig. 3), this was used as the background also in the simulations. Idealized CAOs were then added to the background turbulent heat flux until the integrated November–April heat loss reached the 1999–2009 mean. As several strong and very strong CAO events typically occur every winter, too many moderate events were required to obtain the required integrated heat loss. Hence, the three idealized time series were only constructed based on strong and very strong events: either 18 very strong events early in winter, 18 very strong events late in winter, or 67 strong events distributed evenly throughout the winter (Fig. 4). The remaining atmospheric forcing components were constant, equal to the November–April mean between 1999 and 2009.

3. Evolution of hydrographic properties in the Greenland Sea Gyre

By combining data from all three moorings (section 2a), we obtained near-surface to bottom hydrographic time series in the Greenland Sea Gyre covering the entire 1999–2009 period with only three major data gaps (Fig. 5). Throughout the deployment, the entire water column became warmer and more saline (Figs. 5a,b). This development is consistent with Lauvset et al. (2018) and Brakstad et al. (2019), who documented warming and salinification in the upper 2000 m between 1986 and 2016. Lauvset et al. (2018) attributed this change in properties to the increased temperature and salinity of the AW entering the Nordic seas during the same period (e.g., Holliday et al. 2008; Tsubouchi et al. 2021). AW is advected into the Nordic seas by the Norwegian Atlantic Current, which flows northward to the east of the Greenland Sea Gyre, and densified Atlantic-origin water is returned to the south by the EGC on the western side of the gyre (Fig. 1). The Atlantic-origin water is warmer and more saline than the ambient water in the Greenland Sea, and heat and salt continuously penetrate the gyre between 50- and 1500-m depth (Latarius and Quadfasel 2016).

Lauvset et al. (2018) and Brakstad et al. (2019) only considered data above 2000-m depth, which corresponds to the depth range where the evolution of the Greenland Sea properties can be explained by eddy fluxes from surrounding water masses (Latarius and Quadfasel 2016). Below 2000 m, the water column consists of GSDW that has not been ventilated since deep-reaching convection ceased in the early 1980s (e.g., Meincke et al. 1992; Karstensen et al. 2005; Brakstad et al. 2019). After the GSDW was isolated from the surface, it has only been modified by mixing with deep water masses from the Arctic Ocean through Fram Strait (Somavilla et al. 2013) and from the Norwegian Sea through the Jan Mayen Channel (Østerhus and Gammelsrød 1999). These deep waters are

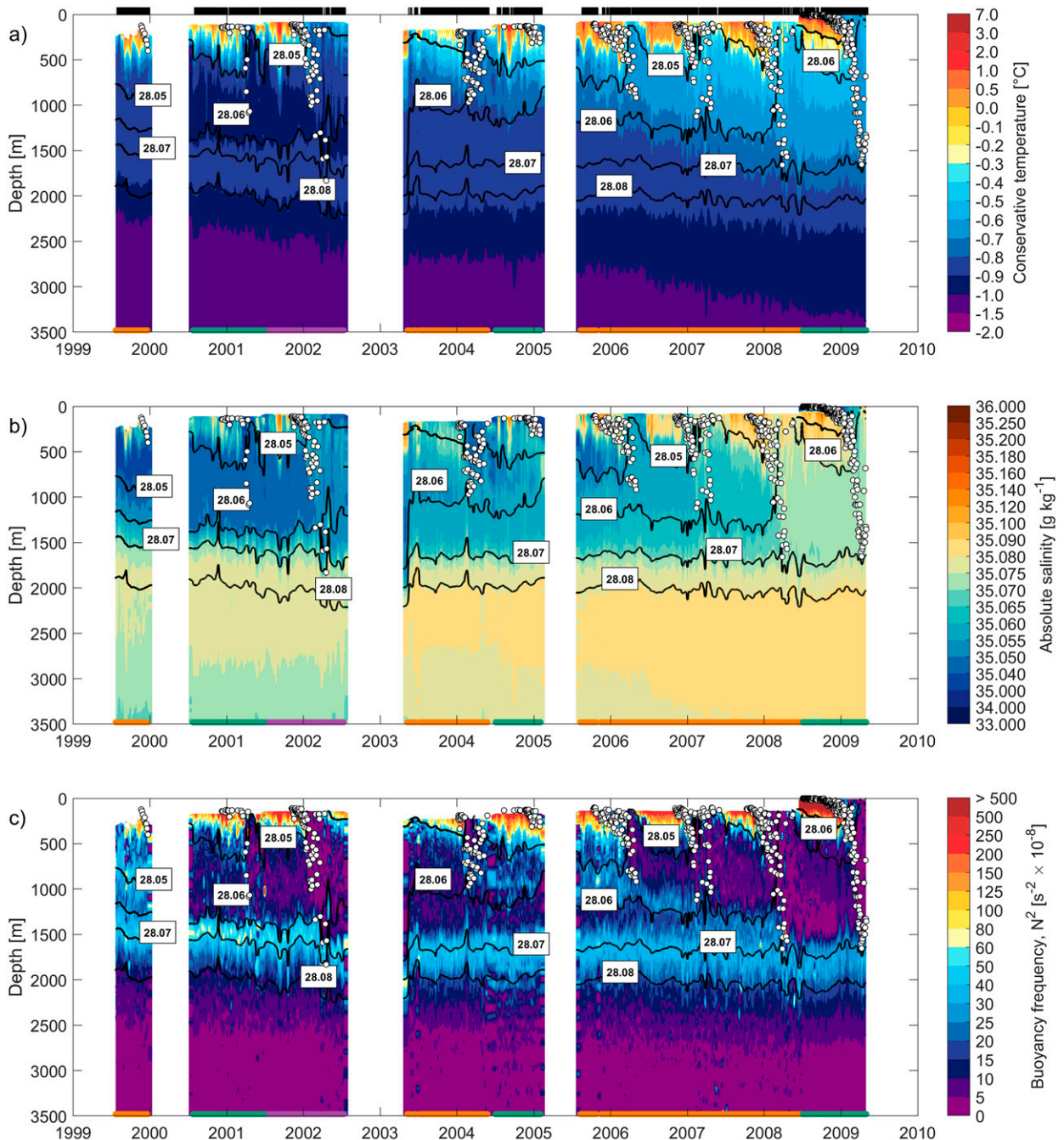


FIG. 5. (a) Temperature, (b) salinity, and (c) buoyancy frequency in the Greenland Sea Gyre between 1999 and 2009. The black lines show potential density contours. Mixed layer depths are marked by white dots. The colors at the bottom of each figure indicate which mooring the data originate from (purple for mooring A, orange for mooring B, and green for mooring C). The x axes indicate the start of each year, while the black bars at the top of the figure mark when profiles were obtained. Note the nonlinear color bars.

warmer and more saline than the GSDW, hence a warming and salinification are observed also at depth (Østerhus and Gammelsrød 1999; Somavilla et al. 2013).

While long-term warming and salinification took place at all depths, the hydrographic properties in the upper half (above 2000 m) of the water column were primarily modified

by local convection in winter. The $\sigma_\theta = 28.05 \text{ kg m}^{-3}$ isopycnal was ventilated every winter, while the $\sigma_\theta = 28.06 \text{ kg m}^{-3}$ isopycnal outcropped during the last two winters (2007/08 and 2008/09, Fig. 5). Thus, convection in the Greenland Sea produced water masses that can supply the densest portion of the overflow water each winter throughout the entire 1999–2009

period (e.g., [Huang et al. 2020](#)). However, the interannual variability in the stratification as indicated by the buoyancy frequency in [Fig. 5c](#) was pronounced. This variability primarily stems from changes in convection depth (indicated by the white dots). Winters of deep convection (such as 2001/02 and 2007/08) were followed by summers of reduced stratification at intermediate depths. The intimate link between convection depth and intermediate stratification was in particular evident in the stepwise increase of convection depth and concurrent decrease in stratification between 2006 and 2009. [Ronski and Budéus \(2005\)](#) used, among other criteria, the change in water column stratification to estimate the depth of wintertime convection by comparing profiles from the Greenland Sea from two subsequent summers. Although we have no measurements from winter 1999/2000, convection to about 1300 m can be inferred from the weakly stratified intermediate layer that appeared in summer 2000. This decrease in stratification from fall 1999 to summer 2000 was caused by convection in winter 1999/2000.

The pronounced stability maximum between 1500- and 2000-m depth separates the GSAIW from the deeper GSDW ([Fig. 5c](#)). This maximum developed following an intermediate temperature maximum around 500 m in the early 1990s (e.g., [Budéus et al. 1998](#); [Karstensen et al. 2005](#)). Since then, the maxima have gradually descended as the overlying GSAIW was ventilated by convection and increased in volume while the GSDW remained isolated from the surface. Even though the temperature maximum disappeared after 2002, the stability maximum persisted around 1500-m depth. Another pronounced intermediate layer of high stratification was evident between 2004 and 2008 (also noted by [Brakstad et al. 2019](#)). This maximum arose around 1000-m depth in 2004 as a result of relatively shallow convection combined with continuous re-stratification from lateral advection across the gyre boundary. Increased convection depths the following winters gradually eroded this stratification maximum until 2008, when it reached 1500-m depth and disappeared.

4. Wintertime mixed layer evolution

Since hydrographic profiles were obtained every second day, it was possible to examine the mixed layer evolution through winter and its response to atmospheric forcing on short time scales. Throughout the record, brief near-surface temperature increases occurred. These events must stem from warmer water masses advected past the moorings as the total heat flux during winter was always directed from the ocean to the atmosphere, hence cooling the ocean. To focus our analysis on the direct impact of the atmospheric forcing on the mixed layer, all profiles with warm near-surface anomalies were excluded from the analysis.

Substantial interannual variability was observed in the end-of-winter mixed layer depths ([Fig. 6a](#)). More than 1000 m separated the shallowest (2005/06) and deepest (2001/02) convection depths. Nevertheless, the mixed layer evolution each winter had a similar pattern both in depth and in temperature ([Figs. 6a,b](#)), which can be divided into two distinct phases. In the first phase (approximately November–January), the shallow mixed layer cooled substantially, even when the heat loss was

only modest, while the change in mixed layer depth was minor ([Fig. 6c](#)). When the mixed layer became sufficiently dense to erode the near-surface stratification that had accumulated through summer, the second phase commenced and the mixed layer deepened rapidly. In the second phase (approximately February–April), the heat loss was distributed over an increasingly deep mixed layer, which led to reduced cooling (i.e., less reduction in temperature); this, however, was not necessarily related to reduced heat fluxes. A similar pattern was noted by [Pawlowicz \(1995\)](#), who investigated the seasonal cycle of temperature and salinity in the upper waters of the Greenland Sea Gyre prior to the 1990s. Hereafter, we refer to the first phase as the cooling phase and the second phase as the deepening phase.

For each winter the transition between the two phases was identified by the inflection point of the 30-day running mean mixed layer depth. The deepening phase commenced when the second derivative had a minimum after mid-December, i.e., when the slope of the mixed layer depth increased the most (marked with diamonds in [Fig. 6a](#)). The transition from the cooling to the deepening phase generally occurred between late December and early February. The winter of 2000/01, when the deepening phase was delayed until mid-March, was an exception. Unlike the other winters, the moorings were covered by sea ice throughout most of January and February. The sea-ice cover insulated the sea surface from the atmosphere, which kept the mixed layer shallow. When the ice edge retreated in March, the water column was exposed to the atmosphere and the deepening phase began shortly thereafter. While the moorings were covered by sea ice, the mixed layer was mostly too shallow to be detected (note the few mixed layers detected between January and February in [Fig. 6a](#)). These under-ice profiles that were not directly exposed to the atmosphere are not included in the analysis.

5. The impact of cold-air outbreaks on the mixed layer

The CAO frequency in winter ranges between 20% and 50% ([Fig. 7](#)). Winters with a high CAO frequency generally have a higher winter mean turbulent heat flux from the ocean to the atmosphere. Corroborating the results of [Papritz and Spengler \(2017\)](#), CAOs accounted for 60%–80% of the total turbulent heat loss each winter. Winter 2001/02 was an exception, then the CAO contribution exceeded 80%, thereby strongly exceeding the range of CAO frequencies (20%–50%, [Fig. 7](#)). Even during winter 2005/06, when the CAO frequency was only 22%, the events were responsible for 60% of the total heat loss. Consistent with the few CAOs this winter, the mean turbulent heat flux was particularly low (107 W m^{-2}), and convection did not exceed 1000 m. There is a clear connection between the winter mean turbulent heat flux and the maximum convection depth each winter, with the deepest mixed layer depths occurring in winters with the strongest atmospheric forcing, hence the incidence of CAOs is important for dense-water formation in the Greenland Sea. Winter 2006/07 breaks the general pattern in [Fig. 7](#). This winter was characterized by strong intermediate stratification in fall ([Fig. 5c](#)), which

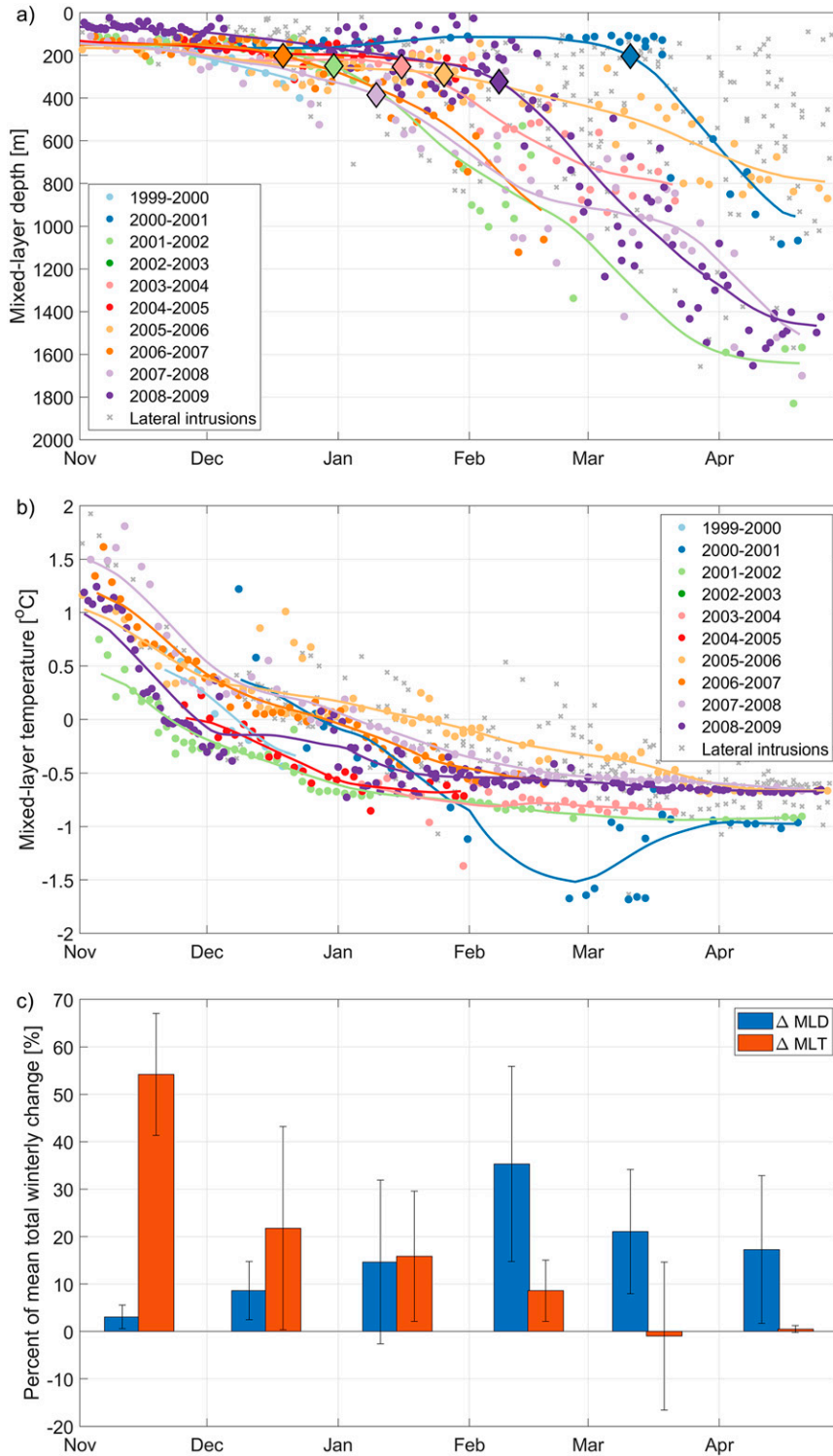


FIG. 6. Wintertime evolution of mixed layer (a) depth and (b) temperature, where each color indicates different winters. The lines are 30-day running means. The gray crosses represent mixed layers that were excluded from the analysis because of lateral intrusions near the surface. The diamonds in (a) indicate the inflection point of the 30-day running mean mixed layer depths (i.e., the transition between the first and the second phases of convection). (c) Mean monthly change in mixed layer depth (MLD) and temperature (MLT), shown as the percentage of the mean (1999–2009) total change from November to April.

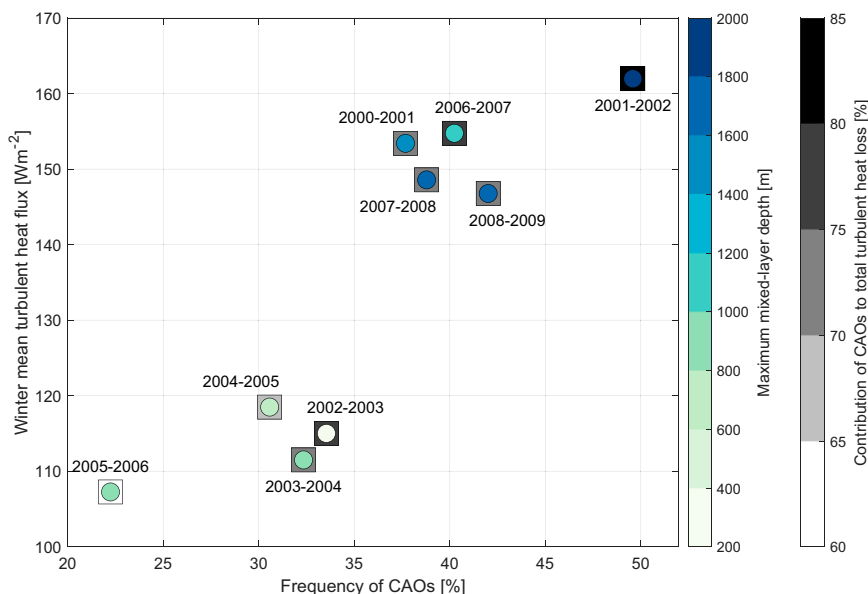


FIG. 7. Winter mean turbulent heat flux plotted as a function of CAO frequency each winter. The maximum convection depth each winter, determined using data from the profiling moorings and from Brakstad et al. (2019), is shown as colored circles, while the contribution of CAOs to the total turbulent heat loss each winter is shown as filled grayscale squares.

constrained the mixed layer to shallower depths than other winters with comparable total heat loss.

Because of sparse temporal data coverage, the direct impact of CAOs on wintertime convection in the Greenland Sea has previously not been quantifiable. Such an analysis is further complicated by the fact that the evolution of the mixed layer through winter is also affected by other factors, such as lateral advection. A recent study from the Iceland Sea investigating the oceanic impact of a single well-observed CAO event, found that the mixed layer response varied spatially depending on the importance of lateral advection (Renfrew et al. 2023). Lateral advection of heat and salt may also vary with time. This implies that the impact of single CAOs on the mixed layer development in the central Greenland Sea may not be representative. However, from our 10-yr moored record with relatively high temporal resolution, a statistical approach yields significant results. The profile-to-profile changes in mixed layer depth and temperature were grouped according to the median value of the CAO index between the profiles (section 2d) and according to the phase they occurred in (Fig. 8). Within each phase and CAO intensity class, outliers that were more than three standard deviations away from the mean were removed.

The impact of a CAO on the mixed layer properties depended on when the event occurred. In the cooling phase, the increase in mixed layer depth was small, even during the strongest CAO events. Regardless of the strength of the CAO, the average deepening rate did not exceed 6 m day^{-1} . In the deepening phase, the rate of increase in mixed layer depth was substantially higher. The deepening also increased with intensifying CAOs, apart from very strong events. Since only three profile-to-profile changes were assigned to very strong CAOs during the deepening phase, this result is not considered statistically

significant. The same analysis was performed using instead the maximum CAO index in the time period between the profiles (not shown). Although the number of data points increased, the mixed layer response was similar to that of strong events. On average, the CAO index exceeded 12 K only 2% of the deepening phase (typically between February and April). The average deepening during strong CAO events was 38 m day^{-1} .

In periods when no CAOs were registered, the mixed layer shoaled. In addition to being cooled by the atmosphere, the water column in the Greenland Sea Gyre is continuously affected by substantial lateral fluxes of heat and salt from surrounding water masses (e.g., Latarius and Quadfasel 2016). The shoaling of the mixed layer indicates that to deepen or maintain the mixed layer, substantial atmospheric forcing is required. During periods characterized by weak atmospheric heat fluxes, lateral fluxes dominate and cause temporary re-stratification and shoaling mixed layers.

While the greatest changes in mixed layer depth occurred in the deepening phase, the mixed layer temperature cooled comparatively little (Fig. 8b). The average change in mixed layer temperature was -0.02 K day^{-1} during strong events. During the cooling phase, on the other hand, changes in the mixed layer temperature were substantial. For strong and very strong CAOs, the mixed layer cooled by $0.07\text{--}0.08 \text{ K day}^{-1}$ on average (due to large standard errors, these two classes were not significantly different).

To summarize, the strong and very strong CAOs that occurred early in winter primarily cooled the mixed layer until the near-surface stratification was eroded and the second phase of convection commenced. In the second phase, the strong atmospheric cooling during CAOs primarily led to a deepening of the mixed layer, while the temperature remained

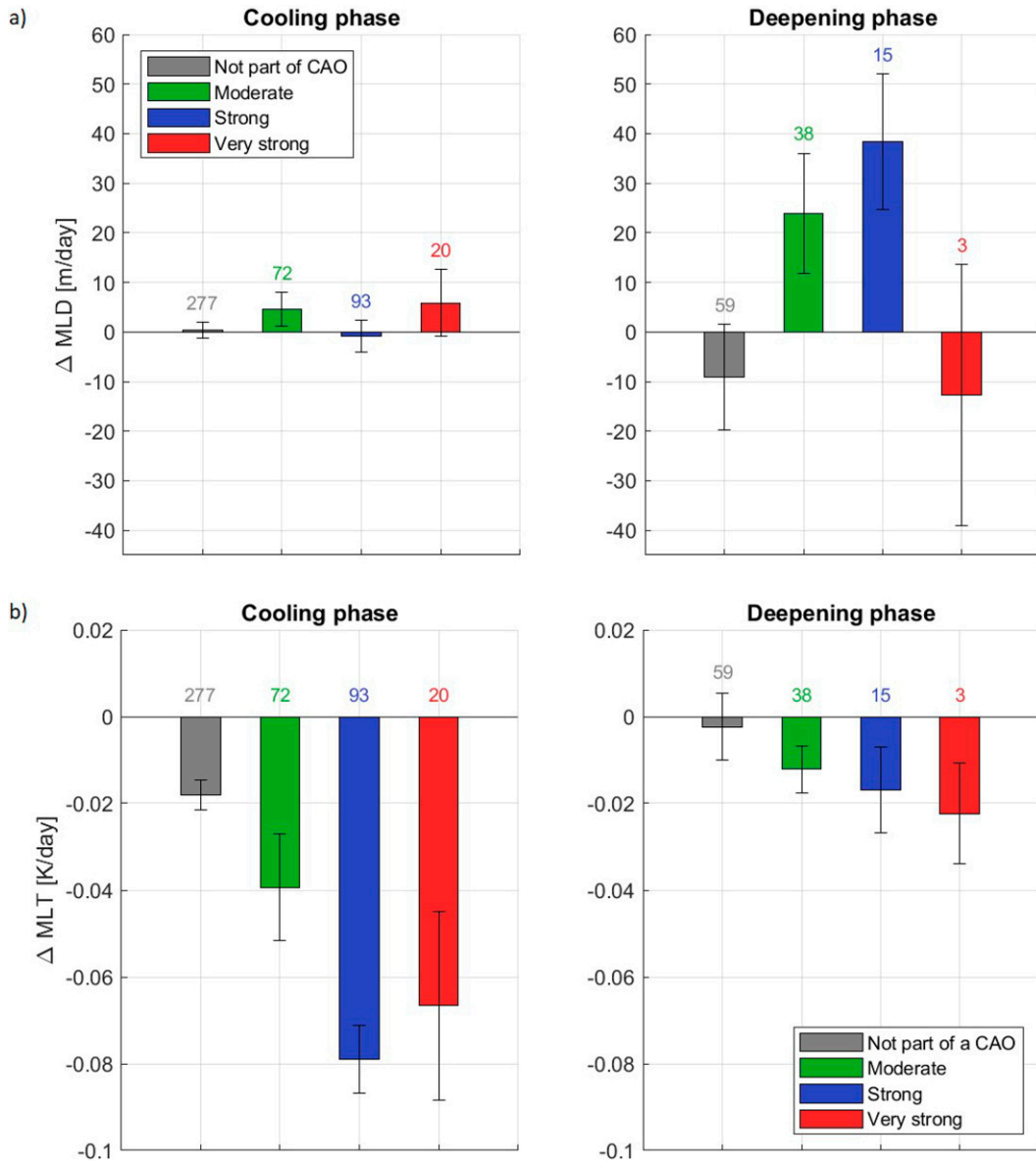


FIG. 8. Daily change in mixed layer (a) depth and (b) temperature calculated from profile-to-profile differences. The changes are grouped by the phase in which they occurred and assigned to a CAO intensity according to the median value of the CAO index in the time period between the profiles (indicated by different colored bars in the figure). The bars mark the average values within each phase and CAO intensity class. The error bars indicate one standard error of the mean, and the number of data points available are written over each bar.

relatively constant. This distinction, in mixed layer response between the two phases, is statistically robust over ten winters.

6. Lateral heat and salt fluxes into the Greenland Sea Gyre

For all CAO-intensity classes, we observed substantial variability in the mixed layer depth and temperature responses as indicated by the large standard errors in Fig. 8. In some cases, the mixed layer shoaled and warmed, even when subject to persistent cooling by the atmosphere. This indicates that

lateral fluxes of heat and salt are also important for the development of the mixed layer. Previous studies have quantified an overall flux of warm and saline water into the Greenland Sea Gyre (Moore et al. 2015; Latarius and Quadfasel 2016; Brakstad et al. 2019), but uncertainties remain regarding the vertical distribution of these fluxes and their origin.

To quantify the lateral heat and salt advection we estimated profile-to-profile differences in temperature and salinity based on the gridded fields shown in Fig. 5. The means over the entire 1999–2009 period were then estimated at each depth level and converted to annual mean rates of change as shown by

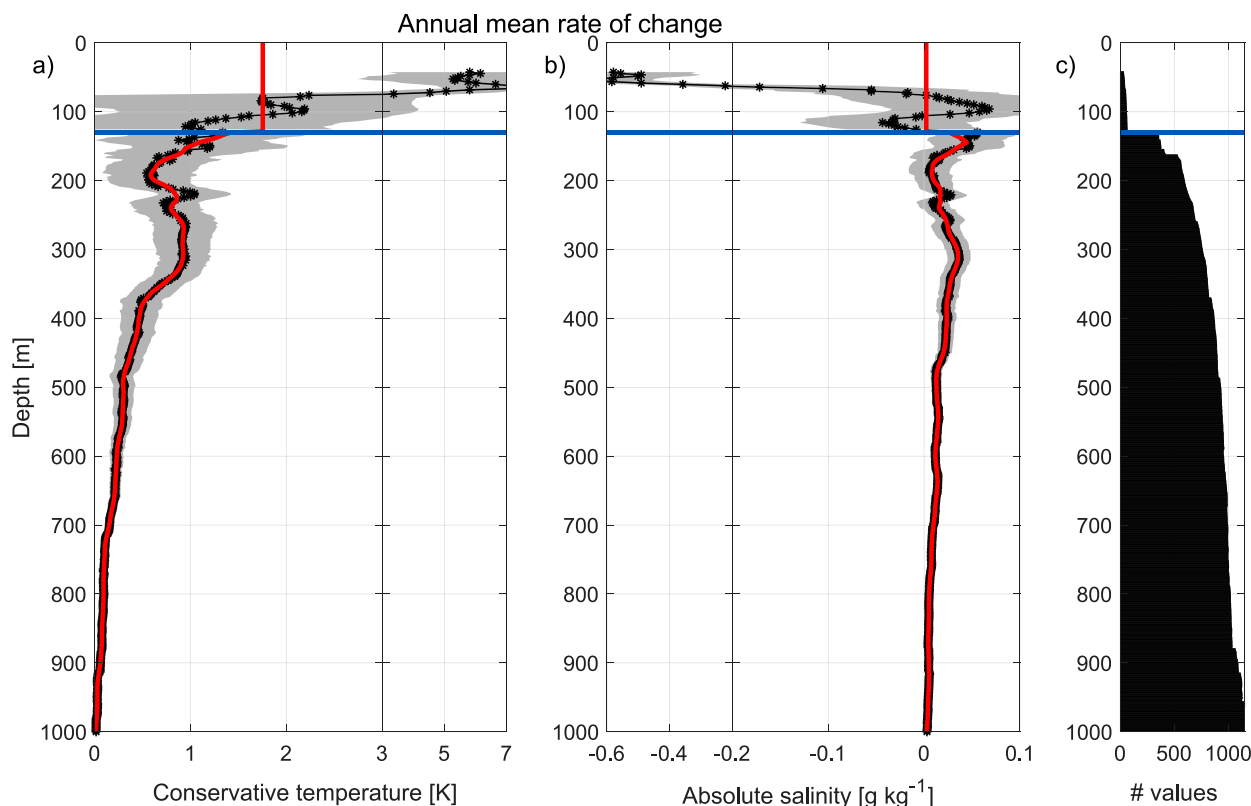


FIG. 9. Annual mean rate of change in (a) temperature and (b) salinity below the surface mixed layer (black profiles). The gray shaded areas indicate one standard error. (c) The number of estimates included in the mean at each depth level. The horizontal blue lines mark 130-m depth. The changes above this depth were estimated based on the shallow profiler only (2008/09) and represent changes observed between May and October since the mixed layer exceeded 130-m depth during winter (November–April). The thick red lines are 30-m running means, and constant from 130 m to the surface (equal to the 70–130-m median values). Note the changing intervals on the x axes.

the black profiles in Fig. 9. All measurements taken within the surface mixed layer were removed to exclude impacts of atmospheric forcing. That is, we assume that any changes in temperature and salinity below the surface mixed layer are caused by lateral advection of heat and salt. The changes above 130 m were estimated based on data from the single deployment of the shallow profiler. These changes are mainly based on summer data (May–October), as the mixed layer depth exceeded 130 m most of the winter.

Atmospheric forcing ignored, the lateral heat flux into the Greenland Sea Gyre (Fig. 9a) would lead to an annual temperature increase of 6 K near the surface, which decreases exponentially toward 0 K at approximately 1000-m depth. Only 4% of the heat added by lateral advection takes place below this depth. In addition to the exponential decrease of the lateral heat fluxes, an intermediate maximum is centered near 300 m. At the same depth level we also observe a maximum in the salt advection (Fig. 9b). The annual change in salinity is generally positive below 130-m depth, while the most prominent signal is the freshening due to inflow of Polar Surface Water in the upper 70 m of the water column.

Relatively warm and saline water is present both east and west of the Greenland Sea Gyre (Fig. 10). The upper part of

the water column in the Norwegian Atlantic Front Current (NAFC) that flows northward along the Mohn Ridge on the eastern side of the gyre contains warm and saline AW. Densified Atlantic-origin water is returned to the south by the EGC on the western side of the gyre and is associated with subsurface maxima in temperature and salinity. Apart from the fresh Polar Surface Water in the west, any lateral exchange between the gyre and its surroundings will lead to an influx of heat and salt into the gyre. Both observations and models indicate that part of the heat and salt in the NAFC crosses the Mohn Ridge into the central Greenland Sea (Spall 2010; Segtnan et al. 2011; Bosse and Fer 2019; Ypma et al. 2020). This could account for the large near-surface heat flux into the gyre, but we do not observe the same surface intensification in salinity (Fig. 9). Instead, the upper part of the gyre is freshened by inflow of Polar Surface Water from the west. The depth of the EGC's subsurface temperature and salinity maxima coincides with the 300-m peaks in annual mean temperature and salinity change within the gyre, suggesting that exchange across the western gyre boundary is the primary source of at least these intermediate maxima. In Fig. 10b, we also see a tongue of saline water reaching the mooring locations from the west.

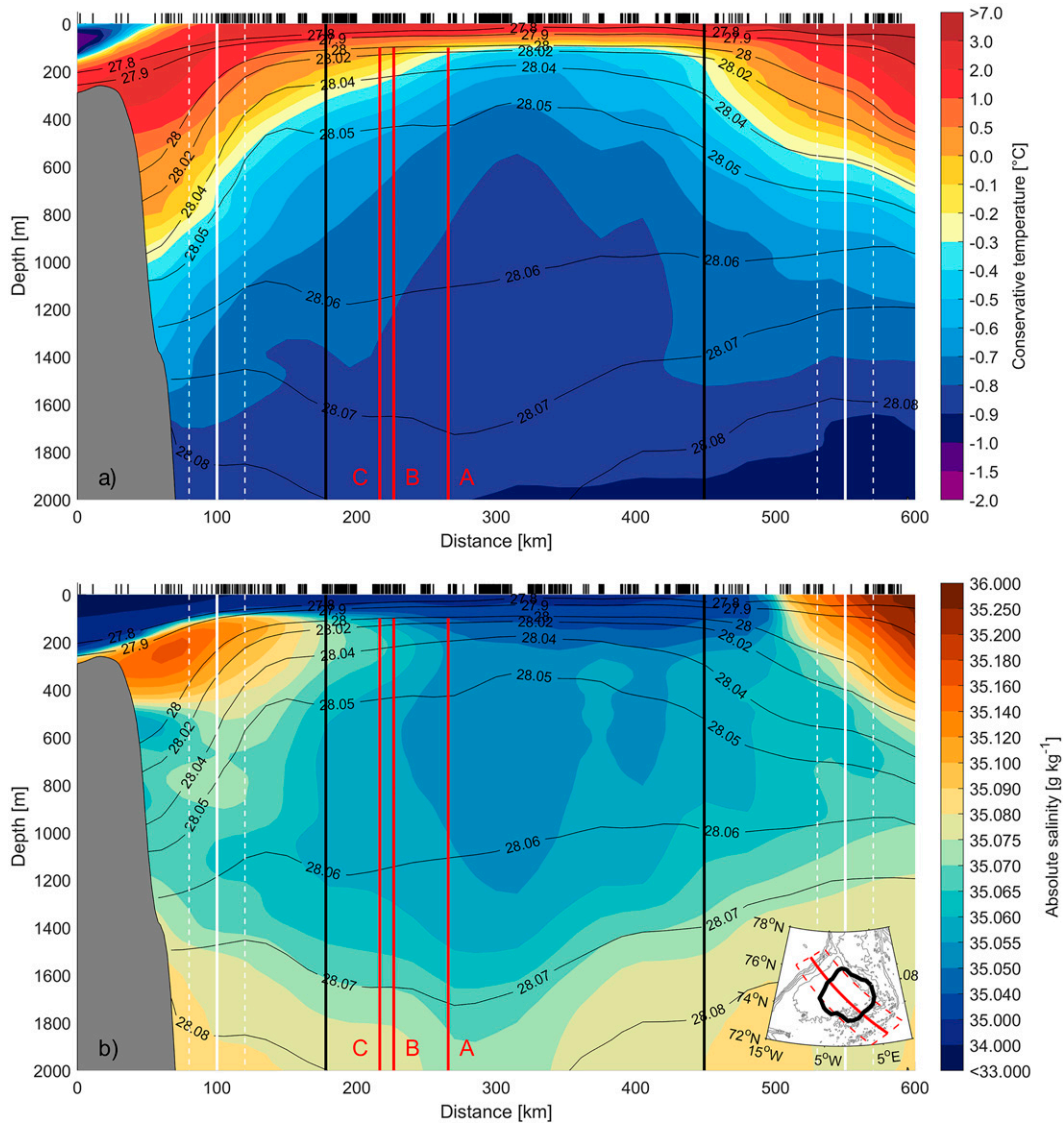


FIG. 10. (a) Temperature and (b) salinity across the Greenland Sea based on shipboard hydrographic measurements and Argo float data from May to October 1999–2012. The black contours indicate potential density. The red solid line in the inserted map in (b) marks the location of the section relative to the gyre (thick black contour). All available observations between the two red dashed lines were included and projected onto the section. The data coverage is indicated by the black bars at the top of each panel, and the x axes show the distance along the section starting from the Greenland shelf. The red vertical lines mark the mooring locations, while the black vertical lines indicate the boundaries of the gyre. Average hydrographic profiles east and west of the gyre were estimated from data within the white dashed lines.

The average temperature and salinity profiles east and west of the Greenland Sea Gyre, as well as the mean hydrography within the gyre, are shown in Fig. 11. The typical density range in the central Greenland Sea between 70- and 500-m depth, where most of the heat and salt are added, is 27.97–28.05 kg m^{-3} . In this density range, when comparing the eastern and western profiles along isopycnals, the temperature and salinity are in fact higher to the west in the EGC. If we assume that exchange of heat and salt primarily

occur along isopycnals, we also see that the gyre is warmer and more saline than the eastern profile in the range 28.02–28.05 kg m^{-3} . Another indication that the exchange across the western gyre boundary dominates is the steepness of the isopycnals, which determines the stability of the frontal boundaries (Spall 2010). The isopycnal steepness is higher on the western side (Fig. 10), which implies that the front is more unstable, and the potential for exchange of heat and salt may be greater.

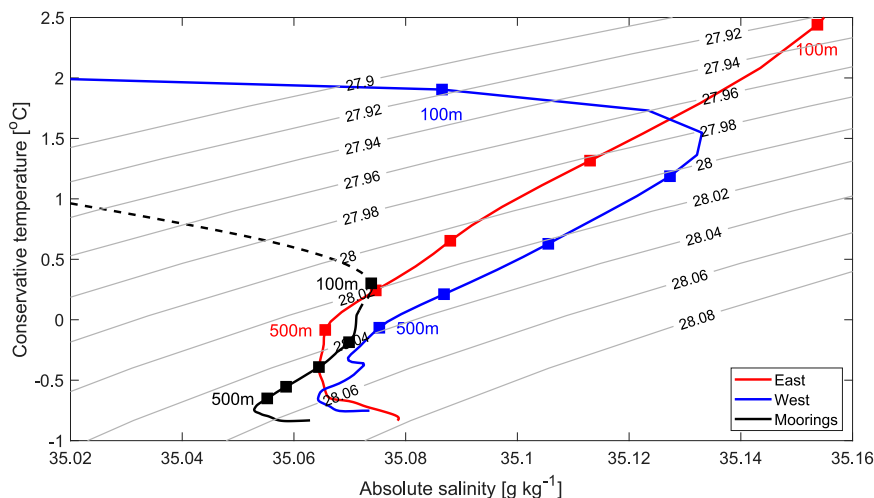


FIG. 11. Average temperature and salinity profiles east (red) and west (blue) of the Greenland Sea Gyre from Fig. 10. The May–October mean temperature and salinity profile within the gyre (black) is based on mooring data between 1999 and 2009. Note that the upper 130 m is from the single deployment of the shallow profiler in 2008–09 (black dashed line). Only data above 1500 m are included in the figure, and every 100-m depth down to 500 m are indicated by colored squares. The gray contours indicate potential density.

7. The impact of lateral advection and the distribution of cold-air outbreaks on the wintertime mixed layer evolution

To determine the impact of lateral advection on the wintertime evolution of the mixed layer, we used the one-dimensional PWP mixed layer model described in section 2e with lateral heat and salt fluxes parameterized. The annual mean rates of temperature and salinity changes (Fig. 9) were converted into rates of changes per model time step of 1 h. These were then added to the simulated temperature and salinity profiles at each time step to represent constant fluxes of heat and salt. No deep convection took place in the simulations with lateral advection parameterized based on the black profiles in Fig. 9 due to the high heat and freshwater fluxes near the surface. The upper 130 m primarily contain summer data, where substantial seasonal variability in lateral advection is expected due to an east–west migration of the Polar Front (Våge et al. 2018; Spall et al. 2021). During fall and winter, the fresh Polar Surface Water is pushed toward the Greenland shelf by westerly Ekman transport induced by strong northerly winds. Hence, we expect a reduced freshwater flux into the central Greenland Sea in winter. To account for this, constant values for rate of change in temperature and salinity (equal to the 70–130-m median values, below the strong freshening signal) were used throughout the upper 130 m as indicated by the red profiles in Fig. 9. The resulting rate of change in depth-integrated heat content corresponds to an influx of 72 W per horizontal square meter, which is approximately 10 W m^{-2} larger than previous gyre-mean estimates (Moore et al. 2015; Latarius and Quadfasel 2016).

For each winter we ran two sets of simulations: one including parameterized lateral heat and salt fluxes and one without lateral advection. Both sets of simulations were initialized using

November hydrographic conditions and forced by ERA5 fluxes from the corresponding winter (section 2e). The simulated development of the mixed layer depth in each run was then compared to observations (i.e., the 30-day running means shown in Fig. 6a). For consistency, we also estimated the 30-day running mean mixed layer depth in each simulation. The mean difference in mixed layer depth between the two sets of simulations and the observations are shown in Fig. 12. The simulations with no lateral advection (the blue dashed line in Fig. 12) always overestimated the mixed layer depth. The seasonal cycle in model error, approaching 800 m in the beginning of March, was due to the timing of the transition between the cooling and deepening phases, which occurred earlier in the model than in the observations. The resulting end-of-winter mixed layer depth was overestimated by 300 m on average when lateral advection was not accounted for. The simulations including advection of heat and salt (the red dashed line in Fig. 12) also overestimated the mixed layer depth, but to a much lesser extent. The deeper mixed layers were mainly caused by an earlier onset of deep convection in the model, which could be explained by the lack of seasonality in the parameterized lateral fluxes. In the mean, the simulated end-of-winter mixed layer depth was underestimated by slightly less than 100 m. Comparing the two sets of simulations, we see that lateral fluxes (of heat, in particular) act to reduce the mixed layer depth in the central Greenland Sea by approximately 400 m on average. That is, the idealized simulations indicate that lateral fluxes are important for the development of the mixed layer in the central Greenland Sea.

The PWP model was also used to investigate the impact of the distribution of CAOs. Three idealized time series of turbulent heat fluxes were created as described in section 2e (Fig. 4), while the remaining atmospheric forcing was kept constant, equal to the winter mean values over the entire 1999–2009

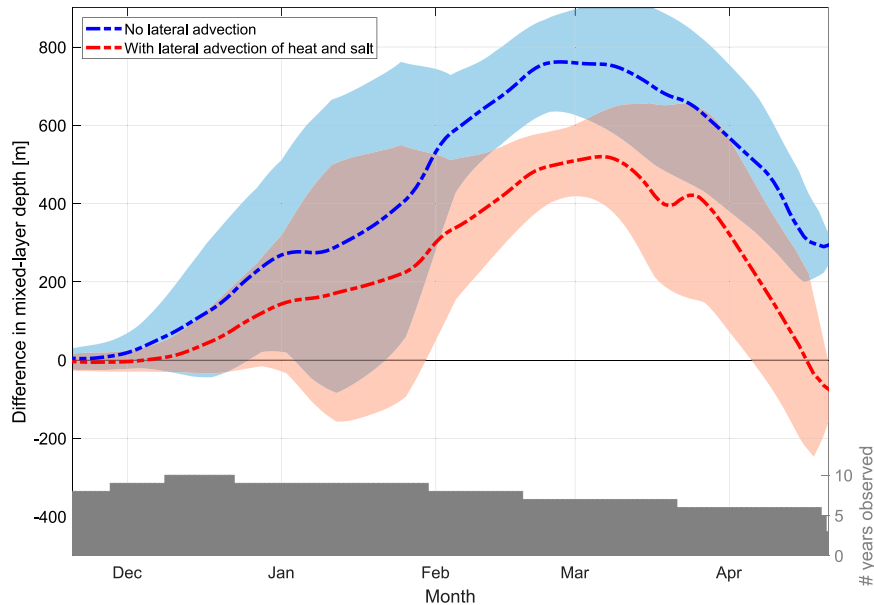


FIG. 12. Simulated minus observed mixed layer depth (30-day running means). The blue dashed line indicates the mean difference for simulations without lateral advection, while the red dashed line is the difference with both heat and salt advection included. The shading, indicating one standard error, represents the variability between the different winters. The gray bars at the bottom of the figure mark the number of years with observations that are compared to the simulations.

period. The turbulent heat flux was either constructed from 1) very strong CAOs concentrated early in the winter, 2) very strong CAOs concentrated late in winter, or 3) strong CAOs evenly distributed over the winter. The integrated turbulent heat losses over the entire winter (November–April) were equal in all three cases, to isolate the effect of the temporal distribution. Simulations were then performed for each winter and set of idealized atmospheric forcing time series, with and without lateral advection.

The simulations suggest that changes in the temporal distribution of CAOs only slightly modify the maximum mixed layer depth and hydrographic properties (Figs. 13a–c). Focusing on the maximum mixed layer depth, we see that very strong CAOs late in winter tend to result in deeper convection than when the events occurred early in winter. However, the difference is only on the order of 100 m. More important are the integrated heat loss over the winter and oceanic lateral advection. The initial hydrographic conditions are also important as indicated by the relatively large winter-to-winter variability (Fig. 13a). The onset of the deepening phase, on the other hand, is greatly influenced by the CAO distribution (Fig. 13d). As expected, more heat loss early in winter leads to an earlier onset of the deepening phase, while the inclusion of lateral advection tends to delay the onset of deep convection.

8. Summary and conclusions

We used a 10-yr (1999–2009) hydrographic record from moored profilers to examine dense-water formation in the Greenland Sea Gyre, with particular focus on the impact of CAOs and lateral fluxes of heat and salt. Although the

moorings were located in the western part of the gyre, the long-term evolution of the mixed layer depth and hydrographic properties were representative for the entire gyre. Consistent with Lauvset et al. (2018) and Brakstad et al. (2019), we observed a general warming and salinification of the entire water column. Intermediate (500–1500 m) convection was observed regularly, and water sufficiently dense ($\sigma_\theta = 28.05 \text{ kg m}^{-3}$) to supply the densest component of the overflow waters was produced every winter (Huang et al. 2020).

In agreement with Papritz and Spengler (2017), we found that between 60% and 80% of the heat lost to the atmosphere during winter occurs during CAOs. Winters with a high frequency of CAOs had the largest winter mean turbulent heat flux and the deepest end-of-winter mixed layer, apart from winter 2006/07 when the intermediate stratification was particularly strong. Our results suggest that the mixed layer development during winter can be divided into two phases: a cooling phase and a deepening phase. The oceanic response to CAOs is highly dependent on which phase the events occur in. Early in winter, the CAOs primarily cooled the mixed layer, while the mixed layer depth remained nearly constant. The magnitude of the cooling depended on the intensity of the events, with the largest cooling ($0.07\text{--}0.08 \text{ K day}^{-1}$) taking place during strong and very strong CAOs. Later in winter, typically between February and April, CAOs mainly deepened the mixed layer. The greatest rate of deepening (up to 38 m day^{-1}) occurred during strong CAOs. Very strong CAOs (with CAO indices above 12 K) rarely occurred in the deepening phase during the 1999–2009 period. It was therefore not possible to obtain statistically meaningful numbers for these events during the deepening phase. The end-of-winter mixed layer depth and hydrographic

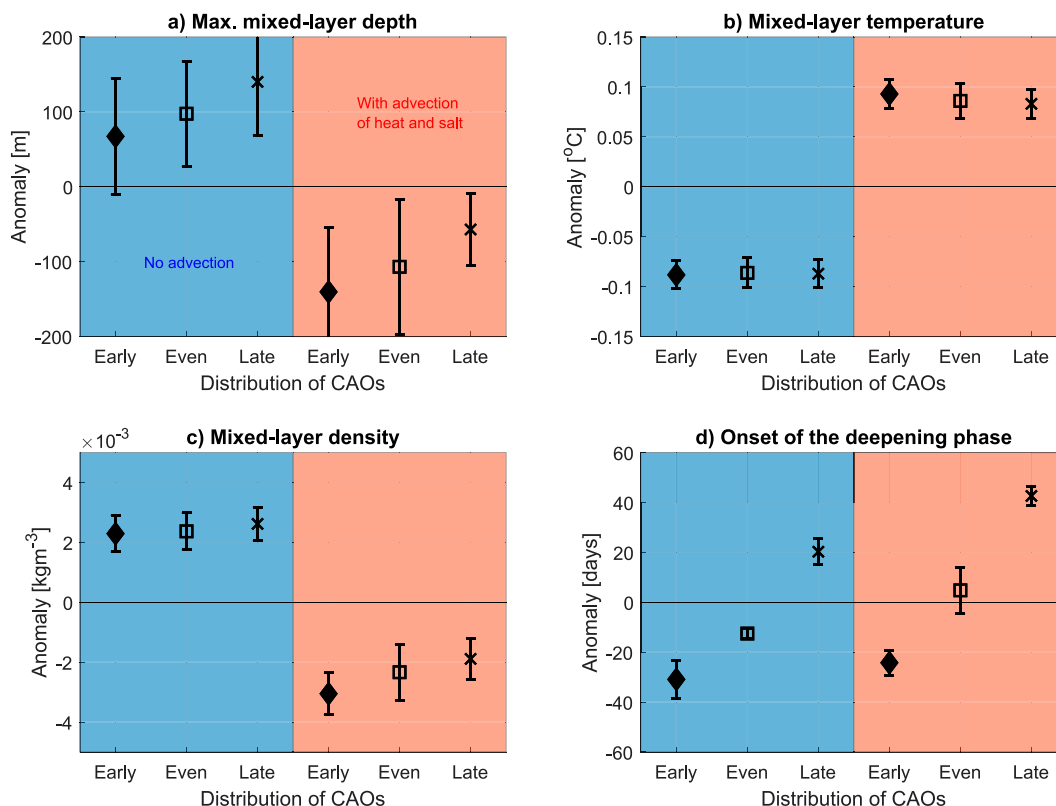


FIG. 13. Anomalies in simulated (a) maximum mixed layer depth, (b) temperature, (c) density, and (d) the onset of the deepening phase, relative to the mean of all simulations each winter. The temporal distribution of CAOs in each simulation is indicated on the x axes, while the background color shows whether lateral advection was included (red) or not (blue). The standard deviations indicate winter-to-winter variability due to different initial hydrographic conditions.

properties are dependent on the integrated heat loss over the winter, but idealized numerical simulations suggest that they are not sensitive to changes in the temporal distribution. The onset of the deepening phase, on the other hand, largely follows the temporal distribution of CAOs: more CAOs early in winter results in an earlier onset of the deepening phase.

A shortcoming of the moored measurements, when considering the atmospheric impact on the mixed layer, is that the profilers did not reach the surface (only to around 100 m depth). The final year of the deployment (2008–09) was an exception. Then a separate moored profiler to sample the upper 130 m of the water column was deployed in addition to the deep profilers. For the remaining years we have only considered the months when the mixed layer exceeded 100-m depth (typically between November and April). When the upper part of the moorings measured a homogeneous layer, we assumed that it was in direct contact with the atmosphere. However, we observed shorter periods of increased temperature near the top of the moorings, even though the atmospheric re-analysis product indicated ocean-to-atmosphere heat loss. Profiles containing such warm-water intrusions were excluded from the statistical analyses, but undetected intrusions above 100-m depth likely occurred. This could account for some of the observed variability in the mixed layer response to CAOs.

The considerable variability in the mixed layer response to CAOs is also in part due to the influx of heat and salt from surrounding water masses. We considered temporal changes in temperature and salinity below the mixed layer to quantify the magnitude and vertical distributions of these fluxes. Our estimated annual mean depth-integrated lateral heat flux of 72 W m^{-2} is comparable to, but approximately 10 W m^{-2} higher than, previous estimates (Moore et al. 2015; Latarius and Quadfasel 2016). This could stem from a lack of winter-time data in our estimate since we excluded measurements taken within the mixed layer, or because we only have one year of near-surface measurements. Unlike Moore et al. (2015) and Latarius and Quadfasel (2016), we included depths below 1500 m in our estimate. However, this is not a main reason for the discrepancy, as less than 4% of the heat added by lateral advection occurs below this depth.

While the largest lateral heat fluxes occur near the surface, we also identified a subsurface maximum near 300-m depth. This maximum corresponds to the depth of the Atlantic-origin water in the East Greenland Current (Håvik et al. 2017), suggesting that it primarily originates from exchange across the western boundary of the gyre. The density structure across the Greenland Sea, based on shipboard hydrographic measurements and Argo float data, also indicate that the western front is more unstable

than the front associated with the Norwegian Atlantic Front Current over the Mohn Ridge. However, the magnitudes of the relative contributions from the regions surrounding the Greenland Sea Gyre remain unknown. Dedicated velocity and turbulence measurements are needed to investigate this further.

The magnitude and vertical distribution of lateral heat and salt fluxes were used in an idealized mixed layer model to determine the impact of lateral advection on the wintertime mixed layer development. The two fluxes have competing effects on the density and depth of the mixed layer. While the lateral heat flux restratifies the water column (leading to a shallower mixed layer), the salt flux preconditions the water column for deeper convection. The combined effect is a reduction in the end-of-winter mixed layer depth by approximately 400 m in the mean relative to simulations without lateral fluxes. Apart from the inflow of fresh Polar Surface Water, the salt flux is positive over the rest of the water column. [Lauvset et al. \(2018\)](#) and [Brakstad et al. \(2019\)](#) found that increased salt advection since the mid-1990s has led to increased mixed layer depths and sustained the formation of GSAIW, even though the atmospheric heat fluxes declined ([Moore et al. 2015](#)). The trend in AW salinity has recently reversed ([Mork et al. 2019](#)), and convection in the Greenland Sea could become increasingly vulnerable to changes in the atmospheric forcing.

The hydrographic measurements from the moored profilers provide a unique dataset, both in terms of high temporal resolution and the long duration, which are both necessary to quantify the direct impact of CAOs on the wintertime mixed layer. This study provides a first demonstration that winter-to-winter variability in CAO frequency has a profound impact on the ocean mixed layer and on dense-water formation in the Greenland Sea. Through a well-established link between variability in seasonal CAO frequency and the frequency of extratropical cyclones ([Fletcher et al. 2016](#); [Papritz and Grams 2018](#)), our results provide an avenue for understanding how seasonal variability in the configuration of the North Atlantic storm track feeds back on dense-water formation in the central Greenland Sea. Our analysis also highlights the importance of the interplay between atmospheric forcing and oceanic lateral advection for the Greenland Sea mixed layer development.

Acknowledgments. This work was funded by the Trond Mohn Foundation under Grant Agreement BFS2016REK01 (KS, AB, and KV), the Bjerknes Centre for Climate Research (KS), the Office of Naval Research Global (Award N62909-22-1-2023, AB and KV), and the Helmholtz Infrastructure Initiative FRAM (WJvA). The authors would also like to thank Dr. Gereon Budéus (Alfred Wegener Institute for Polar and Marine Research) for providing post processed data and for help with the technical description. The mooring time series were funded by the IPY-legacy project LOTEVA-GS.

Data availability statement. The hydrographic data from the moored autonomous profilers, obtained by the Alfred Wegener Institute, are available at <https://doi.pangaea.de/10.1594/PANGAEA.911001> ([Budéus et al. 2020](#)). The hydrographic

dataset from [Brakstad et al. \(2023\)](#) consists of observations from several archives that can be accessed as listed in their Table 1. The combined hydrographic dataset is available at the Norwegian Marine Data Centre (<https://doi.org/10.21335/NMDC-1271328906>). The ERA5 reanalysis can be downloaded from the Copernicus Climate Service (<https://climate.copernicus.eu/climate-reanalysis>).

REFERENCES

- Aagaard, K., J. H. Swift, and E. C. Carmack, 1985: Thermohaline circulation in the Arctic Mediterranean Seas. *J. Geophys. Res.*, **90**, 4833–4846, <https://doi.org/10.1029/JC090iC03p04833>.
- Behrendt, A., H. Sumata, B. Rabe, and U. Schauer, 2018: UDASH - Unified Database for Arctic and Subarctic Hydrography. *Earth Syst. Sci. Data*, **10**, 1119–1138, <https://doi.org/10.5194/essd-10-1119-2018>.
- Bosse, A., and I. Fer, 2019: Mean structure and seasonality of the Norwegian Atlantic Front current along the Mohn Ridge from repeated glider transects. *Geophys. Res. Lett.*, **46**, 13 170–13 179, <https://doi.org/10.1029/2019GL084723>.
- Bracegirdle, T. J., and S. L. Gray, 2008: An objective climatology of the dynamical forcing of polar lows in the Nordic seas. *Int. J. Climatol.*, **28**, 1903–1919, <https://doi.org/10.1002/joc.1686>.
- Brakstad, A., K. Våge, L. Håvik, and G. W. K. Moore, 2019: Water mass transformation in the Greenland Sea during the period 1986–2016. *J. Phys. Oceanogr.*, **49**, 121–140, <https://doi.org/10.1175/JPO-D-17-0273.1>.
- , G. Gebbie, K. Våge, E. Jeansson, and S. R. Ólafsdóttir, 2023: Formation and pathways of dense water in the Nordic seas based on a regional inversion. *Prog. Oceanogr.*, **212**, 102981, <https://doi.org/10.1016/j.pocean.2023.102981>.
- Budéus, G., 2009: Autonomous daily CTD profiles between 3,700 meters and the ocean surface. *Sea Technol.*, **10**, 45–48.
- , W. Schneider, and G. Krause, 1998: Winter convective events and bottom water warming in the Greenland Sea. *J. Geophys. Res.*, **103**, 18 513–18 527, <https://doi.org/10.1029/98JC01563>.
- , K. Ohm, M. Damm, and R. Plugge, 2005: The externally powered, compressibility compensated Jojo mooring: A mechanical solution to autonomous deep sea profiling. *Deep-Sea Res. I*, **52**, 1964–1973, <https://doi.org/10.1016/j.dsr.2005.05.005>.
- , A. Brakstad, K. Svingen, K. Våge, and W.-J. von Appen, 2020: Physical oceanography data from moorings J008-J034 and JP31/JP34 in the Greenland Sea, 1999–2009. PANGAEA, <https://doi.org/10.1594/PANGAEA.910907>.
- Chafik, L., and T. Rossby, 2019: Volume, heat, and freshwater divergences in the subpolar North Atlantic suggest the Nordic seas as key to the state of the meridional overturning circulation. *Geophys. Res. Lett.*, **46**, 4799–4808, <https://doi.org/10.1029/2019GL082110>.
- , H. Hátún, J. Kjellsson, K. M. H. Larsen, T. Rossby, and B. Berx, 2020: Discovery of an unrecognized pathway carrying overflow waters toward the Faroe Bank Channel. *Nat. Commun.*, **11**, 3721, <https://doi.org/10.1038/s41467-020-17426-8>.
- Dahlke, S., A. Solbès, and M. Maturilli, 2022: Cold air outbreaks in Fram Strait: Climatology, trends, and observations during an extreme season in 2020. *J. Geophys. Res. Atmos.*, **127**, e2021JD035741, <https://doi.org/10.1029/2021JD035741>.
- Eldevik, T., J. E. Ø. Nilsen, D. Iovino, K. A. Olsson, A. B. Sandø, and H. Drange, 2009: Observed sources and variability of Nordic seas overflow. *Nat. Geosci.*, **2**, 406–410, <https://doi.org/10.1038/ngeo518>.

- Fletcher, J., S. Mason, and C. Jakob, 2016: The climatology, meteorology, and boundary layer structure of marine cold air outbreaks in both hemispheres. *J. Climate*, **29**, 1999–2014, <https://doi.org/10.1175/JCLI-D-15-0268.1>.
- Harden, B. E., and Coauthors, 2016: Upstream sources of the Denmark Strait overflow: Observations from a high-resolution mooring array. *Deep-Sea Res. I*, **112**, 94–112, <https://doi.org/10.1016/j.dsr.2016.02.007>.
- Håvik, L., R. S. Pickart, K. Våge, D. J. Torres, A. M. Thurnherr, A. Beszczynska-Möller, W. Walczowski, and W.-J. von Appen, 2017: Evolution of the East Greenland current from Fram Strait to Denmark Strait: Synoptic measurements from summer 2012. *J. Geophys. Res. Oceans*, **122**, 1974–1994, <https://doi.org/10.1002/2016JC012228>.
- , M. Almansi, K. Våge, and T. W. N. Haine, 2019: Atlantic-origin overflow water in the East Greenland current. *J. Phys. Oceanogr.*, **49**, 2255–2269, <https://doi.org/10.1175/JPO-D-18-0216.1>.
- Helland-Hansen, B., and F. Nansen, 1909: The Norwegian Sea: Its physical oceanography based upon the Norwegian researches, 1900–1904. Norwegian Fishery and Marine Investigations Rep., Vol. 2, 390 pp., <https://hdl.handle.net/11250/114874>.
- Hersbach, H., and Coauthors, 2020: The ERA5 global reanalysis. *Quart. J. Roy. Meteor. Soc.*, **146**, 1999–2049, <https://doi.org/10.1002/qj.3803>.
- Holliday, N. P., and Coauthors, 2008: Reversal of the 1960s to 1990s freshening trend in the northeast North Atlantic and Nordic seas. *Geophys. Res. Lett.*, **35**, L03614, <https://doi.org/10.1029/2007GL032675>.
- Huang, J., R. S. Pickart, R. X. Huang, P. Lin, A. Brakstad, and F. Xu, 2020: Sources and upstream pathways of the densest overflow water in the Nordic seas. *Nat. Commun.*, **11**, 5389, <https://doi.org/10.1038/s41467-020-19050-y>.
- IOC, SCOR, and IAPSO, 2010: The international thermodynamic equation of seawater 2010: Calculation and use of thermodynamic properties. Intergovernmental Oceanographic Commission, Manuals and Guides No. 56, UNESCO, 218 pp., https://www.teos-10.org/pubs/TEOS-10_Manual.pdf.
- Jeansson, E., S. Jutterström, B. Rudels, L. G. Anderson, K. Anders Olsson, E. P. Jones, W. M. Smethie, and J. H. Swift, 2008: Sources to the East Greenland current and its contribution to the Denmark Strait overflow. *Prog. Oceanogr.*, **78**, 12–28, <https://doi.org/10.1016/j.pocean.2007.08.031>.
- , A. Olsen, and S. Jutterström, 2017: Arctic intermediate water in the Nordic seas, 1991–2009. *Deep-Sea Res. I*, **128**, 82–97, <https://doi.org/10.1016/j.dsr.2017.08.013>.
- Karstensen, J., P. Schlosser, D. W. Wallace, J. L. Bullister, and J. Blindheim, 2005: Water mass transformation in the Greenland Sea during the 1990s. *J. Geophys. Res.*, **110**, C07022, <https://doi.org/10.1029/2004JC002510>.
- Kolstad, E. W., 2011: A global climatology of favourable conditions for polar lows. *Quart. J. Roy. Meteor. Soc.*, **137**, 1749–1761, <https://doi.org/10.1002/qj.888>.
- Latarius, K., and D. Quadfasel, 2010: Seasonal to inter-annual variability of temperature and salinity in the Greenland Sea Gyre: Heat and freshwater budgets. *Tellus*, **62A**, 497–515, <https://doi.org/10.1111/j.1600-0870.2010.00453.x>.
- , and —, 2016: Water mass transformation in the deep basins of the Nordic seas: Analyses of heat and freshwater budgets. *Deep-Sea Res. I*, **114**, 23–42, <https://doi.org/10.1016/j.dsr.2016.04.012>.
- Lauvset, S. K., A. Brakstad, K. Våge, A. Olsen, E. Jeansson, and K. A. Mork, 2018: Continued warming, salinification and oxygenation of the Greenland Sea gyre. *Tellus*, **70A**, 1–9, <https://doi.org/10.1080/16000870.2018.1476434>.
- Lorbacher, K., D. Dommenget, P. P. Niiler, and A. Köhl, 2006: Ocean mixed layer depth: A subsurface proxy of ocean-atmosphere variability. *J. Geophys. Res.*, **111**, C07010, <https://doi.org/10.1029/2003JC002157>.
- Lozier, M. S., and Coauthors, 2019: A sea change in our view of overturning in the subpolar North Atlantic. *Science*, **363**, 516–521, <https://doi.org/10.1126/science.aau6592>.
- Malmberg, S. A., 1983: Hydrographic investigations in the Iceland and Greenland Seas in late winter 1971. *Jokull*, **33**, 133–140.
- Marshall, J., and F. Schott, 1999: Open-ocean convection: Observations, theory and models. *Rev. Geophys.*, **37**, 1–64, <https://doi.org/10.1029/98RG02739>.
- Mauritzen, C., 1996: Production of dense overflow waters feeding the North Atlantic across the Greenland-Scotland Ridge. Part 1: Evidence for a revised circulation scheme. *Deep-Sea Res. I*, **43**, 769–806, [https://doi.org/10.1016/0967-0637\(96\)00037-4](https://doi.org/10.1016/0967-0637(96)00037-4).
- Meinke, J., and Coauthors, 1990: Greenland Sea Project: A venture toward improved understanding of the oceans' role in climate. *Eos, Trans. Amer. Geophys. Union*, **71**, 750–756, <https://doi.org/10.1029/90EO00208>.
- , S. Jónsson, and J. H. Swift, 1992: Variability of convective conditions in the Greenland Sea. *ICES Mar. Sci. Symp.*, **195**, 32–39.
- , B. Rudels, and H. J. Friedrich, 1997: The Arctic Ocean-Nordic seas thermohaline system. *ICES J. Mar. Sci.*, **54**, 283–299, <https://doi.org/10.1006/jmsc.1997.0229>.
- Moore, G. W. K., K. Våge, R. S. Pickart, and I. A. Renfrew, 2015: Decreasing intensity of open-ocean convection in the Greenland and Iceland Seas. *Nat. Climate Change*, **5**, 877–882, <https://doi.org/10.1038/nclimate2688>.
- , —, I. A. Renfrew, and R. S. Pickart, 2022: Sea-ice retreat suggests re-organization of water mass transformation in the Nordic and Barents Seas. *Nat. Commun.*, **13**, 67, <https://doi.org/10.1038/s41467-021-27641-6>.
- Mork, K. A., Ø. Skagseth, and H. Sjøiland, 2019: Recent warming and freshening of the Norwegian Sea observed by Argo data. *J. Climate*, **32**, 3695–3705, <https://doi.org/10.1175/JCLI-D-18-0591.1>.
- Nilsen, J. E. Ø., and E. Falck, 2006: Variations of mixed layer properties in the Norwegian Sea for the period 1948–1999. *Prog. Oceanogr.*, **70**, 58–90, <https://doi.org/10.1016/j.pocean.2006.03.014>.
- Østerhus, S., and T. Gammelsrød, 1999: The abyss of the Nordic seas is warming. *J. Climate*, **12**, 3297–3304, [https://doi.org/10.1175/1520-0442\(1999\)012<3297:TAOTNS>2.0.CO;2](https://doi.org/10.1175/1520-0442(1999)012<3297:TAOTNS>2.0.CO;2).
- , and Coauthors, 2019: Arctic Mediterranean exchanges: A consistent volume budget and trends in transports from two decades of observations. *Ocean Sci.*, **15**, 379–399, <https://doi.org/10.5194/os-15-379-2019>.
- Papritz, L., and T. Spengler, 2017: A Lagrangian climatology of wintertime cold air outbreaks in the Irminger and Nordic seas and their role in shaping air-sea heat fluxes. *J. Climate*, **30**, 2717–2737, <https://doi.org/10.1175/JCLI-D-16-0605.1>.
- , and C. M. Grams, 2018: Linking low-frequency large-scale circulation patterns to cold air outbreak formation in the north-eastern North Atlantic. *Geophys. Res. Lett.*, **45**, 2542–2553, <https://doi.org/10.1002/2017GL076921>.
- , S. Pfahl, H. Sodemann, and H. Wernli, 2015: A climatology of cold air outbreaks and their impact on air-sea heat fluxes in the high-latitude South Pacific. *J. Climate*, **28**, 342–364, <https://doi.org/10.1175/JCLI-D-14-00482.1>.

- Pawlowicz, R., 1995: A note on seasonal cycles of temperature and salinity in the upper waters of the Greenland Sea Gyre from historical data. *J. Geophys. Res.*, **100**, 4715–4726, <https://doi.org/10.1029/94JC02014>.
- Petit, T., M. S. Lozier, S. A. Josey, and S. A. Cunningham, 2020: Atlantic deep water formation occurs primarily in the Iceland Basin and Irminger Sea by local buoyancy forcing. *Geophys. Res. Lett.*, **47**, e2020GL091028, <https://doi.org/10.1029/2020GL091028>.
- Pickart, R. S., D. J. Torres, and R. A. Clarke, 2002: Hydrography of the Labrador Sea during active convection. *J. Phys. Oceanogr.*, **32**, 428–457, [https://doi.org/10.1175/1520-0485\(2002\)032<0428:HOTLSD>2.0.CO;2](https://doi.org/10.1175/1520-0485(2002)032<0428:HOTLSD>2.0.CO;2).
- Price, J. F., R. A. Weller, and R. Pinkel, 1986: Diurnal cycling: Observations and models of the upper ocean response to diurnal heating, cooling, and wind mixing. *J. Geophys. Res.*, **91**, 8411–8427, <https://doi.org/10.1029/JC091iC07p08411>.
- Renfrew, I. A., and Coauthors, 2023: Coupled atmosphere-ocean observations of a cold air outbreak and its impact on the Iceland Sea. *Quart. J. Roy. Meteor. Soc.*, **149**, 472–493, <https://doi.org/10.1002/qj.4418>.
- Ronski, S., and G. Budéus, 2005: Time series of winter convection in the Greenland Sea. *J. Geophys. Res.*, **110**, C04015, <https://doi.org/10.1029/2004JC002318>.
- Segtnan, O. H., T. Furevik, and A. D. Jenkins, 2011: Heat and freshwater budgets of the Nordic seas computed from atmospheric reanalysis and ocean observations. *J. Geophys. Res.*, **116**, C11003, <https://doi.org/10.1029/2011JC006939>.
- Semper, S., K. Våge, R. S. Pickart, H. Valdimarsson, D. J. Torres, and S. Jónsson, 2019: The emergence of the North Icelandic Jet and its evolution from northeast Iceland to Denmark Strait. *J. Phys. Oceanogr.*, **49**, 2499–2521, <https://doi.org/10.1175/JPO-D-19-0088.1>.
- , R. S. Pickart, K. Våge, K. M. H. Larsen, B. Hansen, and H. Hátún, 2020: The Iceland-Faroe slope jet: A conduit for dense water toward the Faroe Bank Channel overflow. *Nat. Commun.*, **11**, 5390, <https://doi.org/10.1038/s41467-020-19049-5>.
- Somavilla, R., 2019: Draining and upwelling of Greenland Sea deep waters. *J. Geophys. Res. Oceans*, **124**, 2842–2860, <https://doi.org/10.1029/2018JC014249>.
- , U. Schauer, and G. Budéus, 2013: Increasing amount of Arctic Ocean deep waters in the Greenland Sea. *Geophys. Res. Lett.*, **40**, 4361–4366, <https://doi.org/10.1002/grl.50775>.
- Spall, M. A., 2010: Non-local topographic influences on deep convection: An idealized model for the Nordic seas. *Ocean Modell.*, **32**, 72–85, <https://doi.org/10.1016/j.ocemod.2009.10.009>.
- , M. Almansi, J. Huang, T. W. Haine, and R. S. Pickart, 2021: Lateral redistribution of heat and salt in the Nordic seas. *Prog. Oceanogr.*, **196**, 102609, <https://doi.org/10.1016/j.pocean.2021.102609>.
- Strass, V. H., E. Fahrback, U. Schauer, and L. Sellmann, 1993: Formation of Denmark Strait overflow water by mixing in the East Greenland current. *J. Geophys. Res.*, **98**, 6907–6919, <https://doi.org/10.1029/92JC02732>.
- Terpstra, A., I. A. Renfrew, and D. E. Sergeev, 2021: Characteristics of cold-air outbreak events and associated polar mesoscale cyclogenesis over the North Atlantic region. *J. Climate*, **34**, 4567–4584, <https://doi.org/10.1175/JCLI-D-20-0595.1>.
- Tsubouchi, T., K. Våge, B. Hansen, K. M. H. Larsen, S. Østerhus, C. Johnson, S. Jónsson, and H. Valdimarsson, 2021: Increased ocean heat transport into the Nordic seas and Arctic Ocean over the period 1993–2016. *Nat. Climate Change*, **11**, 21–26, <https://doi.org/10.1038/s41558-020-00941-3>.
- Våge, K., R. S. Pickart, M. A. Spall, H. Valdimarsson, S. Jónsson, D. J. Torres, S. Østerhus, and T. Eldevik, 2011: Significant role of the North Icelandic Jet in the formation of Denmark Strait overflow water. *Nat. Geosci.*, **4**, 723–727, <https://doi.org/10.1038/ngeo1234>.
- , —, —, G. W. K. Moore, H. Valdimarsson, D. J. Torres, S. Y. Erofeeva, and J. E. Ø. Nilsen, 2013: Revised circulation scheme north of the Denmark Strait. *Deep-Sea Res. I*, **79**, 20–39, <https://doi.org/10.1016/j.dsr.2013.05.007>.
- , G. W. Moore, S. Jónsson, and H. Valdimarsson, 2015: Water mass transformation in the Iceland Sea. *Deep-Sea Res. I*, **101**, 98–109, <https://doi.org/10.1016/j.dsr.2015.04.001>.
- , L. Papritz, L. Håvik, M. A. Spall, and G. W. K. Moore, 2018: Ocean convection linked to the recent ice edge retreat along East Greenland. *Nat. Commun.*, **9**, 1287, <https://doi.org/10.1038/s41467-018-03468-6>.
- , S. Semper, H. Valdimarsson, S. Jónsson, R. S. Pickart, and G. W. K. Moore, 2022: Water mass transformation in the Iceland Sea: Contrasting two winters separated by four decades. *Deep-Sea Res. I*, **186**, 103824, <https://doi.org/10.1016/j.dsr.2022.103824>.
- Visbeck, M., J. Fischer, and F. Schott, 1995: Preconditioning the Greenland Sea for deep convection: Ice formation and ice drift. *J. Geophys. Res.*, **100**, 18 489–18 502, <https://doi.org/10.1029/95JC01611>.
- Ypma, S. L., S. Georgiou, J. S. Dugstad, J. D. Pietrzak, and C. A. Katsman, 2020: Pathways and water mass transformation along and across the Mohn-Knipovich ridge in the Nordic seas. *J. Geophys. Res. Oceans*, **125**, e2020JC016075, <https://doi.org/10.1029/2020JC016075>.